

Quasinormal modes of spherically symmetric black hole with cosmological constant and global monopole in bumblebee gravity

Yenshembam Priyobarta Singh^a, Irengbam Roshila Devi^a, Telem Ibungochouba Singh^a

^a*Department of Mathematics, Manipur University, Canchipur, Imphal, 795003, Manipur, India*

Abstract

This paper studies the scalar, electromagnetic field and Dirac field perturbations of spherically symmetric black hole within the framework of Einstein-bumblebee gravity model with global monopole and cosmological constant. We investigate the effective potentials, greybody factors and quasinormal modes (QNMs) by applying the Klein-Gordon equation, electromagnetic field equation and Dirac equation expressed in Newman-Penrose (NP) formalism. Using the general method of rigorous bound, the greybody factors of scalar, electromagnetic and Dirac field are derived. Applying the sixth order WKB approximation and Padé approximation, the QNM frequencies are derived. We also discuss the impact of global monopole η , cosmological constant Λ and Lorentz violation parameter L to the effective potential, greybody factor and QNMs. Increasing the parameter η prevents the rise of effective potential for both Schwarzschild-de Sitter (SdS)-like and Schwarzschild-Anti de Sitter (SAdS)-like black holes with global monopole and consequently increases the greybody factors. However, decreasing the parameter L reduces the rise of effective potential for the SAdS-like black hole with global monopole and it increases the greybody factor but increasing the parameter L has an opposite effect for SdS-like black hole with global monopole. It is also shown that the shadow radius increases with increasing the parameter η for both dS and AdS cases. Increasing the value of L tends to increase the shadow radius for dS black hole but it has an opposite effect in AdS case. A careful studying is being carried out to investigate how the absorption cross-section gets affected when the parameter L appears into the picture.

Keywords: Effective potential, Quasinormal modes, Greybody factors, Bumblebee gravity, Absorption cross-section

1. Introduction

General Relativity is a theory which describes the gravitation at the classical level and is also plagued with the appearance of singularities. The standard model of particle physics has explained the other three fundamental interactions at the quantum front. A comprehensive understanding of the natural world can be obtained by using these two theories. Therefore, the unification of these two models is fundamental and its findings give us a better comprehension of nature. The perturbations of black hole theory plays a very important role in the exploration of quasinormal modes (QNMs). Ref. [1] discussed an innovative work on the black hole perturbation and the outcome of this study will provide a foundation for a plethora of other important research works. If a black hole is subjected to non radial perturbation, it oscillates with complex frequency at the intermediate stage. This oscillation is known as QNMs. The real part of QNMs is the oscillation frequency of the perturbation and the imaginary part is connected to damping [2]. Ref. [3] discussed the QNMs in the simulation of gravitational wave scattering of a Schwarzschild space time. The QNMs represent the oscillation frequencies which heavily rely on the black hole parameters like mass, charge and spin [4, 5]. The results derived from the electromagnetic spectra [6, 7] combined with gravitational waves will be able to investigate the fundamental parameters like mass, angular momentum and charge of the black hole, which in turn may be able to test the theory of gravity at the strong field limit. Since the observation of gravitational waves by LIGO and Virgo, a lot of interest has been paid in the study of QNMs. Many methods have been developed for

Email addresses: priyoyensh@gmail.com (Yenshembam Priyobarta Singh), roshilairengbam@gmail.com (Irengbam Roshila Devi), ibungochouba@rediffmail.com (Telem Ibungochouba Singh)

calculating the QNMs such as WKB method [8–11], analytical method [12, 13], Frobenius method [14], continued fraction method [15], Mashhoon method [16]. Hawking [17] showed that the black holes emit particles as well as absorb, scatter and radiate when quantum gravity effect is taken into consideration. This emission is later known as Hawking radiation that interacts with the curvature of spacetime around the black hole event horizon when it leaves from the event horizon, accordingly altering its properties. An observer located at infinity cannot detect the usual black body spectrum [18, 19]. A measure of variation between the black body spectrum and the rescaled spectrum is defined by the greybody factor. The greybody factor also represents a transmission coefficient in the scattering of black hole when the spacetime behaves the role of a potential barrier. There are several methods for calculating the greybody factors such as matching technique [20, 21], WKB approximation method for high gravitational potential [22, 23] and rigorous bound method [24–27].

There exists a great deal of uncertainty to determine the fundamental black hole parameters precisely, which gives us a lot of space for developing another modified gravity theory [28]. The bumblebee gravity along with the other modified theories will be of particular interest, in which the Lorentz symmetry violation involves a non zero expectation value of a bumblebee field, if a suitable potential is taken into consideration. The Lorentz symmetry gives a fundamental symmetry for the derivation of any physically possible theories. The development of standard model of particle physics and general relativity are based on the Lorentz symmetry. These two theories have explained the known physical occurrences in the universe within the achievable energy range. The recent advances in unified gauge theories and the confirmation from high energy cosmic ray [29, 30] proposed that Lorentz symmetry, which is taken as fundamental to quantum gravity theory and general relativity, break in physics at the high energy Planck scale 10^{19} GeV. Recently, some research works showed that the signal connected to Lorentz symmetry violation may precisely exhibit at lower energy level, which led to the discovery of their corresponding consequence in experiment [31]. Some observations which break the Lorentz symmetry at low energy residual effects of Planck scale are Cosmic rays [32, 33], Photon tests [34, 35], Muon tests [36, 37], Meson tests [38–40], Clock comparison experiments [41, 42]. Moreover, the Lorentz symmetry violation in the field of string theory, electrodynamics and non-abelian theory have been discussed in [43–45]. Since then, many researchers have studied the Lorentz symmetry violation in different types of spacetimes [46–51].

One of the important theories which includes the Lorentz symmetry violation is known as the Einstein-bumblebee gravity [52, 53]. The prototype of the bumblebee model, a string inspired framework featuring tensor-induced Lorentz symmetry violation has been discussed in [52, 54]. A potential $V(B^a B_a)$ acting on a vector field B_a gives the spontaneous Lorentz symmetry violation in the frame of Bumblebee gravity [55]. Refs. [56–63] investigated the properties of bumblebee model in Riemann and Riemann-Cartan spacetimes. An exact Schwarzschild-like black hole in the bumblebee gravity model has been derived by Casana et al. [64]. Since then, many researchers have investigated the bumblebee gravity model in different types of spacetimes such as traversable wormhole solution [65], slowly rotating Kerr-like black holes [66], Schwarzschild-like black holes with cosmological constant [53] and other solutions [67–75].

Furthermore, data which involve the Lorentz violation theory have been derived and were also retained in the black hole shadow [66, 76], the black hole superradiance [77], the accretion disc [78] and the motion of massive body [58]. The use of quasi-periodic oscillation frequencies obtained from the observation data (GRO J1655-40, XTE J1550-564) and GRS1915+105 showed that the range of Lorentz spontaneous symmetry breaking becomes constrained for the rotating black hole within the bumblebee gravity model [79–81]. It is noted from the Grand Unified Theories that the global monopole is a special class of topological defect which may be developed in the early universe after the spontaneous breaking of symmetry of the global $O(3)$ symmetry to $U(1)$ [82]. The unusual property possessed by global monopole is a solid deficit angle, which makes the black hole with a global monopole topologically different and also leads to an interesting outcome in the physical consequence [83, 84]. Ref. [85] derived an exact Schwarzschild-like black hole solution with global monopole in bumblebee gravity and studied the effect of global monopole and bumblebee field on photon sphere and black hole shadow.

The shadow cast by a Schwarzschild black hole is initially investigated by Synge [86]. The influence of a thin accretion disc on the shadow of black hole is investigated by Luminet [87]. The shadow of rotating Kerr black hole is also studied by Bardeen [88]. After taking the direct image of M87* at the core of the Virgo A galaxy and SgrA* at the core of the Milky Way Galaxy [89, 90], many researchers have paid a lot of interest in the study of black hole shadow. The internal structures of the black hole cannot be studied directly due to their special properties. The

black hole interacts with the surrounding environment, such as scattering, absorption and Hawking radiation. This gives the information about the internal structure of the black hole. To study the absorption cross-section as one of the interactions is very important. The most efficient and useful way to understand the black hole properties is to study the matter wave absorption and test the field around black holes. Since then many researchers [91–105] studied the absorption cross-section in different black hole spacetimes. In this connection, the paper aims to investigate the effects of monopole parameter η and Lorentz violation parameter L in the greybody factor, QNMs, shadow radius and absorption cross-section of spherically symmetric black hole.

The paper is organised as follows: In Section 2, we discuss some properties of SdS/AdS-like black hole with global monopole. We discuss the perturbation of scalar, electromagnetic field and Dirac field and the corresponding effective potentials of the black hole are also derived in Section 3. In section 4, the greybody factors from the scalar, electromagnetic and Dirac fields are derived. In section 5, the quasinormal mode frequencies for scalar, electromagnetic and Dirac perturbations have been derived by using WKB 6th order and Padé approximation for the different black hole parameters. We discuss the shadow radius in Section 6 and high energy absorption cross section in Section 7. Conclusion is given in Section 8.

2. Schwarzschild-like black hole with global monopole and cosmological constant

The line element of Schwarzschild-like black hole with global monopole and cosmological constant in bumblebee gravity is given by [109]

$$ds^2 = f(r)dt^2 - \left(\frac{1+L}{f(r)}\right)dr^2 - r^2 d\theta^2 - r^2 \sin^2 \theta d\varphi^2, \quad (1)$$

where $f(r)$ has the form

$$f(r) = 1 - \kappa\eta^2 - \frac{2M}{r} - \frac{(1+L)\Lambda r^2}{3}, \quad (2)$$

where M is the mass of the black hole, L is the Lorentz violating parameter, $\kappa = 8\pi$, Λ is the cosmological constant and η is the global monopole parameter. Clearly in the limiting value of $L \rightarrow 0$, Eq. (1) reduces to the line element of SdS/AdS black hole with global monopole. If $\eta = 0$, the resulting metric reduces to the line element of SdS/AdS-like black hole in bumblebee gravity [53]. Moreover if $\Lambda = 0$, we recover the line element of Schwarzschild-like black hole with global monopole [85]. The expression for the black hole mass M is obtained from $f(r) = 0$ as

$$M = \frac{r}{6} \left\{ 3(1 - \kappa\eta^2) - (1+L)r^2\Lambda \right\}. \quad (3)$$

It is noticed that $f(r) \rightarrow -\infty$ as $r \rightarrow 0$. Further, as $r \rightarrow \infty$, $f(r) \rightarrow \pm\infty$ according to the positive or negative cosmological constant provided. For AdS case, $f(r)$ keeps on increasing but for dS case i.e. $\Lambda > 0$, the value of $f(r)$ increases at first and then decreases. It is to be noted that there is only one positive real horizon for AdS case. However, for dS case, in order to get two positive real horizons, the maximum value of $f(r)$ must be positive. The maximum point of $f(r)$ is achieved at $r = r_m = \left\{ \frac{3M}{\Lambda(1+L)} \right\}^{1/3}$. The condition for having two positive real horizons for dS case is obtained as

$$(1 - \kappa\eta^2)^3 > 9M^2\Lambda(1+L). \quad (4)$$

The event horizon r_e and the cosmological horizon r_c for dS spacetime are given by

$$r_e = 2 \sqrt{\frac{1 - \kappa\eta^2}{\Lambda(1+L)}} \cos\left(\frac{\pi + \Phi}{3}\right), \quad (5)$$

$$r_c = 2 \sqrt{\frac{1 - \kappa\eta^2}{\Lambda(1+L)}} \cos\left(\frac{\pi - \Phi}{3}\right), \quad (6)$$

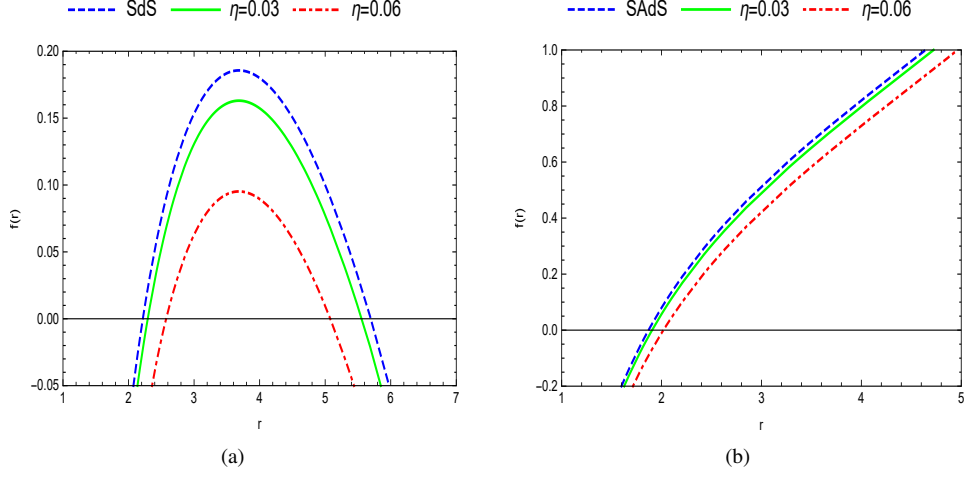


Figure 1: Variation of the metric function of the Schwarzschild-dS/AdS with global monopole under bumblebee gravity model. The physical parameters are chosen as (a) $M = 1$, $\Lambda = 0.05$ and (b) $M = 1$, $\Lambda = -0.05$.

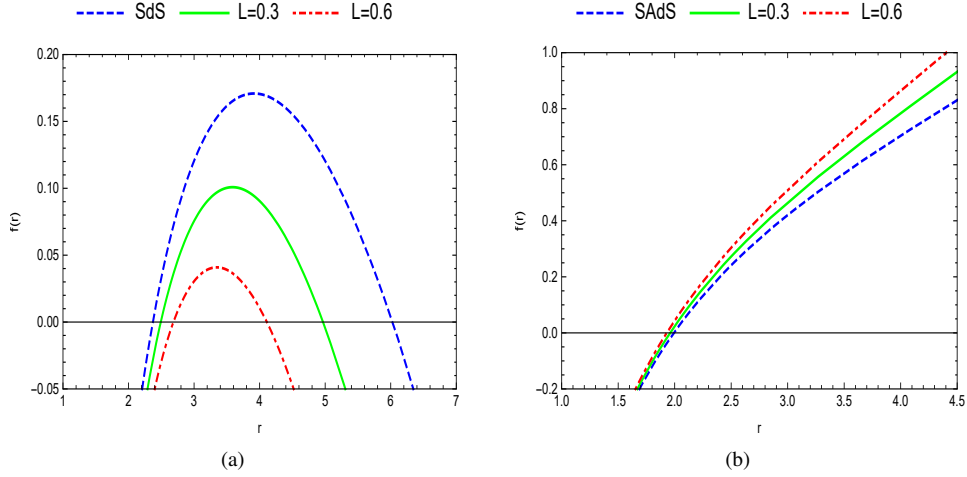


Figure 2: Variation of the metric function of the Schwarzschild-dS/AdS with global monopole under bumblebee gravity model. The physical parameters are chosen as (a) $M = 1$, $\Lambda = 0.05$ and (b) $M = 1$, $\Lambda = -0.05$.

where $\Phi = \cos^{-1} \left[\frac{3M \sqrt{\Lambda(1+L)}}{\sqrt{(1-\kappa\eta^2)^3}} \right]$.

Figs. 1 and 2 illustrate the behaviour of metric function for both dS and AdS spacetimes for different values of monopole parameter and Lorentz violation parameter respectively. For SAdS-like black hole, there is only one horizon (event) and the horizon radius increases with increasing the global monopole parameter and Lorentz violation parameter. Further, it is evident from Fig. 1 that for SdS-like black hole, there are two horizons: event horizon and cosmological horizon. Increasing the global monopole parameter and Lorentz violation parameter increase the distance between the horizons.

3. Scalar, electromagnetic and Dirac perturbations

Black hole perturbation is a useful tool to study small disturbances in black hole spacetime. The study of black hole perturbation is important in understanding the black hole stability, the emission of gravitational waves, Hawking evaporation and the intricate dynamics of extreme astrophysical environments. Black hole perturbation arises due to scalar, electromagnetic, gravitational or Dirac field. When black hole interacts with its surrounding it undergoes perturbation thereby emitting gravitational waves and the waves are detected by observatories like LIGO and Virgo. The study of perturbations of black hole under Bumblebee gravity model has gained interest among researchers to explore the modifications to the gravitational wave propagation and quasinormal mode. Different types of perturbation for different black holes are widely studied in [72–75, 107–109]. In our work, we will study the perturbation of each field separately by assuming the perturbing one field does not affect the background of the other fields.

3.1. Scalar perturbation

The evolution of the scalar field is governed by the Klein-Gordon equation, which is given by [106, 110]

$$\frac{1}{\sqrt{-g}}\partial_\mu\left(\sqrt{-g}g^{\mu\nu}\partial_\nu\Psi\right)=0, \quad (7)$$

where $g^{\mu\nu}$ and g are the inverse of the metric tensor and determinant of the metric tensor. Since the line element (1) represents a static and spherically symmetric metric, the radial and angular parts can be separated by choosing

$$\Psi(t, r, \theta, \phi) = e^{-i\omega t} R(r) Y_{lm}(\theta, \phi), \quad (8)$$

where $Y_{lm}(\theta, \phi)$ are the standard scalar spherical harmonics.

The radial part of Eq. (7), reduces to a one-dimensional Schrödinger-like equation as

$$\frac{d^2\Psi_h}{dr_*^2} + (\omega^2 - V_s(r))\Psi_h = 0, \quad (9)$$

where r_* is the tortoise coordinate defined by

$$dr_* = \frac{\sqrt{1+L}}{f(r)} dr \quad (10)$$

and $V_s(r)$ is the effective potential for the perturbation due to scalar field which is derived as

$$V_s(r) = f(r) \left\{ \frac{l(l+1)}{r^2} + \frac{2M}{(1+L)r^3} - \frac{2\Lambda}{3} \right\}. \quad (11)$$

Fig. 3 shows the variation of effective potential of scalar field perturbation for different values of monopole parameter. Here blue dashed line represents the effective potential of scalar field perturbation for SdS-like/SAdS-like black hole in the absence of monopole parameter. For dS case, it is observed from Fig. 3a that the effective potential vanishes at the event horizon (r_e), cosmological horizon (r_c) and another additional point r_a respectively. The vanishing of the effective potential at the horizons is clearly evident since $f(r)$ appears as a factor in the effective potential. The additional zero point r_a is the point where the second factor in the RHS Eq. (11) becomes zero. Since η doesn't appear in the second factor, the third vanishing point (r_a) remains the same for all the values of η (see Fig. 3a). For AdS case, Λ is negative, so the second factor of the effective potential is strictly positive. Therefore the vanishing point of the effective potential is only at the point where $f(r)$ vanishes i.e. at event horizon. For both dS and AdS cases, the local maximum of the effective potential tends to decrease as the monopole parameter increases. Further, the effective potential of dS case acts as a decreasing function of η in the range $r_e < r < r_a$ but in the range $r_a < r$, it acts as an increasing function of η . However, for AdS case the effective potential behaves as a decreasing function of η . To discuss the results analytically, we take the derivative of V_s with respect to η as

$$\frac{dV_s}{d\eta} = -2\kappa\eta\Sigma_1, \quad (12)$$

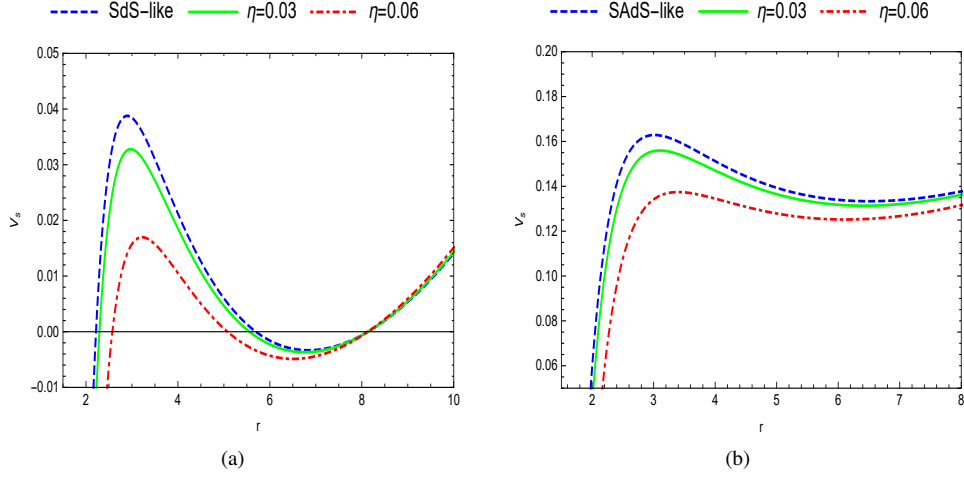


Figure 3: Graphs of the effective potential of the scalar field perturbation: (a) SdS-like black hole ($\Lambda = 0.05$) and (b) SAdS-like black hole ($\Lambda = -0.05$) for different values of global monopole. The physical parameters are chosen as $M = 1$, $l = 1$ and $L = 0.2$.

where $\Sigma_1 = \frac{l(l+1)}{r^2} + \frac{2M}{(1+L)r^3} - \frac{2\Lambda}{3}$. For dS case, one can clearly see that V_s is a decreasing or increasing function of η according to $\Sigma_1 > 0$ or $\Sigma_1 < 0$. Therefore, in the region $r_e < r < r_a$, V_s is a decreasing function of η but in the region $r_a < r$, it is an increasing function. However, for AdS case, V_s is a decreasing function of η in the entire range since $\Sigma_1 > 0$. The findings are consistent with the graphical results obtained in Fig. 3.

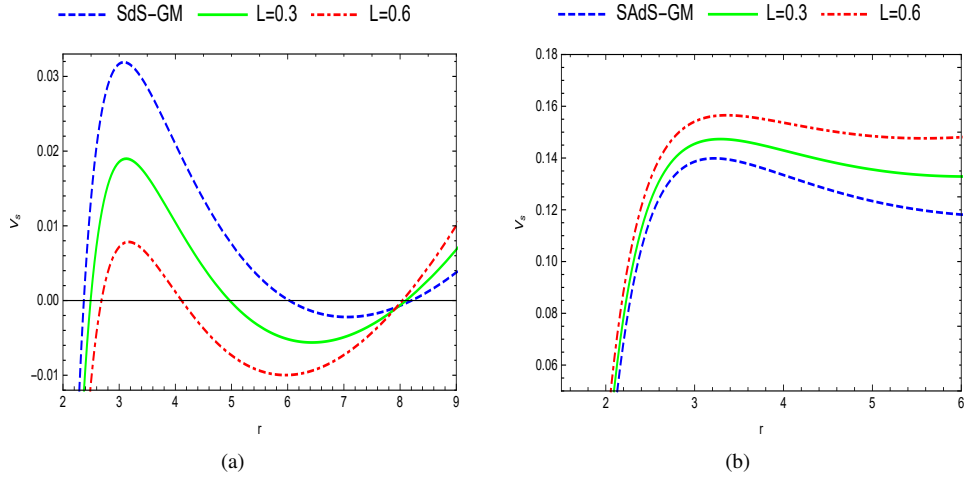


Figure 4: Graphs of the effective potential of the scalar field perturbation: (a) SdS-like black hole with global monopole ($\Lambda = 0.05$) and (b) SAdS-like black hole with global monopole ($\Lambda = -0.05$) for different values of Lorentz violation parameter L . The physical parameters are chosen as $M = 1$, $l = 1$ and $\eta = 0.05$.

In order to see the effect of bumblebee gravity on the effective potential, we illustrate the behaviour of effective potential in Fig. 4 by varying Lorentz violation parameter and fixing other parameters. The blue dashed line in Figs. 4a and 4b represent the original SdS and SAdS black hole with global monopole. For dS case, the local maximum of the effective potential decreases with increasing the Lorentz violation parameter but for AdS case the effect is opposite. The effective potential V_s decreases with increasing L in between the event horizon and the additional zero point r_a for the dS case. However, it behaves as an increasing function of L when $r > r_a$. Therefore, in the region

between the event horizon and the cosmological horizon, when the Lorentz violation parameter increases in the dS case, less wave energy is being communicated to the surrounding medium which is an indication of higher greybody factors. Conversely, in the case of AdS, raising the Lorentz violation parameter traps more wave energy, which lowers the greybody factors. To examine the above results analytically we calculate

$$\frac{dV_s}{dL} = \Sigma_2 = \frac{4M^2}{(1+L)^2 r^4} + \frac{2r^2 \Lambda^2}{9} - \frac{2(1-\kappa\eta^2)}{(1+L)^2 r^3} - \frac{l(l+1)\Lambda}{3}. \quad (13)$$

From Eq. (13), one can clearly see that for both dS and AdS cases, Σ_2 can be positive or negative according to the choice of the values of black hole parameters. Thus, according to the range of r and the choice of the black hole parameter, the effective potential may increase or decrease with increasing L which is consistent with Fig. 4a.

3.2. Electromagnetic perturbation

In this subsection, we will study the electromagnetic field perturbation of Schwarzschild dS/AdS black hole with global monopole in the bumblebee gravity.

The electromagnetic field in curved spacetime follows the equation [111]

$$\frac{1}{\sqrt{-g}} \partial_\nu (\sqrt{-g} g^{\mu\alpha} g^{\nu\beta} F_{\alpha\beta}) = 0, \quad (14)$$

where the Maxwell tensor is $F_{\mu\nu} = \partial_\mu A_\nu - \partial_\nu A_\mu$ and A_μ is a four dimensional vector potential. In the Regge-Wheeler-Zerilli formalism, one may decompose A_μ in terms of the scalar and vector spherical harmonics

$$A_\mu = \sum_{l,m} e^{-i\omega t} \left(\begin{bmatrix} 0 \\ o \\ a^{lm}(r) \mathbf{S}_{lm} \end{bmatrix} + \begin{bmatrix} j^{lm}(r) Y_{lm} \\ h^{lm}(r) Y_{lm} \\ k^{lm}(r) \mathbf{Y}_{lm} \end{bmatrix} \right), \quad (15)$$

where Y_{lm} are the scalar spherical harmonics and the vector spherical harmonics (\mathbf{S}_{lm} and \mathbf{Y}_{lm}) are defined as

$$\mathbf{S}_{lm} = \begin{pmatrix} \frac{1}{\sin \theta} \partial_\varphi Y_{lm} \\ -\sin \theta \partial_\theta Y_{lm} \end{pmatrix}, \quad \mathbf{Y}_{lm} = \begin{pmatrix} \partial_\theta Y_{lm} \\ \partial_\varphi Y_{lm} \end{pmatrix}, \quad (16)$$

where ω is the frequency. Here l and m denote the angular momentum quantum number and the azimuthal number respectively. The first term in the right hand side of Eq. (15) represents the axial mode while the second term represents the polar mode. It's important to note that the axial and polar modes have parity $(-1)^{l+1}$ and $(-1)^l$ respectively. Moreover, the polar and axial parts have equal contributions to the final result [112, 113]. Thus, we focus only on the axial part. Now, substituting Eq. (15) in Eq. (14) and applying tortoise coordinate r_* , the radial part of Eq. (14) can be written in the form of Schrödinger like wave form as

$$\frac{d^2 a^{lm}}{dr_*^2} + (\omega^2 - V_h(r)) a^{lm} = 0, \quad (17)$$

where

$$V_m(r) = f(r) \times \frac{l(l+1)}{r^2}. \quad (18)$$

To analyse the effect of η on the effective potential of electromagnetic field perturbation, we plot V_m of dS and AdS cases for different values of η in Figs. 5a and 5b respectively. Both the effective potentials of dS and AdS vanish at the horizons. In contrast to the effective potential of scalar perturbation, which vanishes at three points, the electromagnetic perturbation's effective potential vanishes at only two points in the dS case. Increasing the values of monopole parameter the effective potential reduces in both dS and AdS cases. Thus, the monopole parameter η enhances the flow of waves to the surrounding in the electromagnetic field perturbation. This suggests the greybody

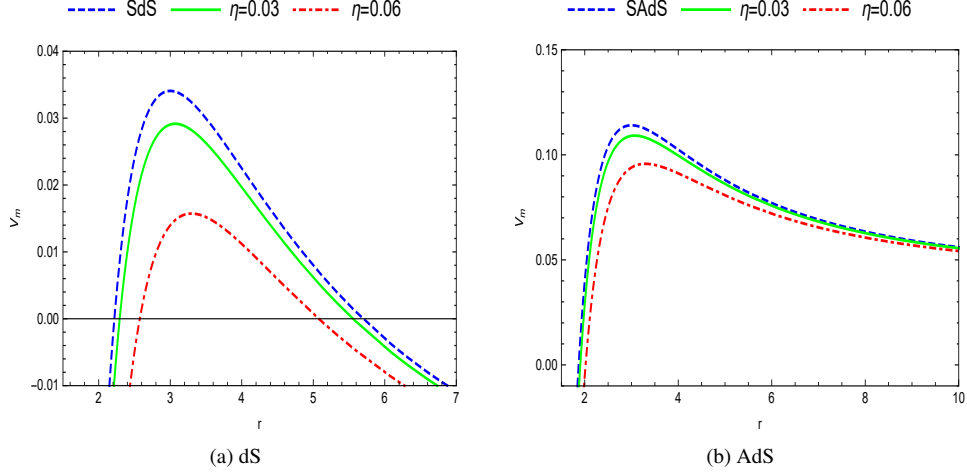


Figure 5: Graphs of the effective potential of the electromagnetic field perturbation: (a) SdS-like black hole ($\Lambda = 0.05$) and (b) SAdS-like black hole ($\Lambda = -0.05$) for different values of global monopole. The physical parameters are chosen as $M = 1$, $l = 1$ and $L = 0.2$.

factor of the electromagnetic perturbation will get higher with increasing the monopole parameter. Further, we will also analyse the nature of the effective potential analytically. From Eq. (18), we calculate

$$\frac{dV_m}{d\eta} = \frac{-2\kappa\eta l(1+l)}{r^2}. \quad (19)$$

From Eq. (19), it is clearly evident that for both the dS and AdS cases, the effective potential V_m is a decreasing function of η .

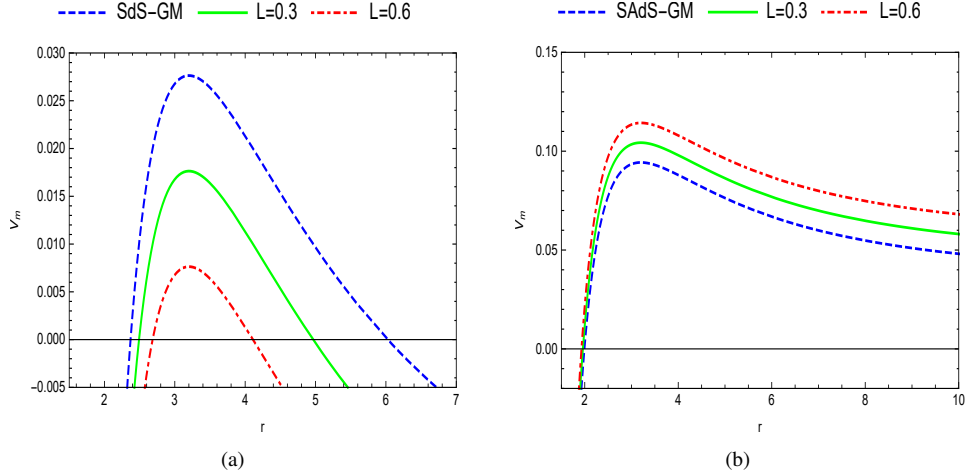


Figure 6: Graphs of the effective potential of the electromagnetic field perturbation: (a) SdS-like black hole ($\Lambda = 0.05$) and (b) SAdS-like black hole ($\Lambda = -0.05$) for different values of Lorentz violation parameter. The physical parameters are chosen as $M = 1$, $l = 1$ and $\eta = 0.05$.

The nature of the effective potential of electromagnetic perturbation for dS and AdS for different values of L are illustrated in Figs. 6a and 6b respectively. For dS case, the effective potential decreases with increasing the Lorentz violation parameter. Since the potential barrier reduces as L increases, more waves are transmitted, thereby indicating the rise of greybody factor. However for AdS case, the potential barrier increases with increasing the Lorentz violation

parameter L . Thus the effect of Lorentz violation parameter on the effective potential of electromagnetic perturbation of dS and AdS cases are completely opposite. This opposite effect can be also observed from the analytical analysis of V_m . The derivative of V_m with respect to L can be derived from Eq. (18) as

$$\frac{dV_m}{dL} = -\frac{l(1+l)\Lambda}{3}. \quad (20)$$

We observe that according to the sign of Λ , dV_m/dL can be either positive or negative. Thus, V_m is a decreasing function in dS case but it is an increasing function in AdS case.

3.3. Dirac perturbation

In this section, we will discuss the massless and massive Dirac perturbation of SdS/SAdS-like black hole in global monopole using the NP formalism. In NP formalism, the Chandrasekhar-Dirac equation (CDE) is given by [114]

$$\begin{aligned} (D + \epsilon - \rho)B_1 + (\bar{\delta} + \pi - \alpha)B_2 &= i\mu^* C_1, \\ (\delta + \beta - \tau)B_1 + (\Delta + \mu - \gamma)B_2 &= i\mu^* C_2, \\ (D + \bar{\epsilon} - \bar{\rho})C_2 - (\delta + \bar{\pi} - \bar{\alpha})C_1 &= i\mu^* B_2, \\ (\Delta + \bar{\mu} - \bar{\gamma})C_1 - (\bar{\delta} + \bar{\beta} - \bar{\tau})C_2 &= i\mu^* B_1, \end{aligned} \quad (21)$$

where B_1 , B_2 , C_1 and C_2 represent the Dirac spinors and $D = l^\mu \partial_\mu$, $\Delta = n^\mu \partial_\mu$, $\delta = m^\mu \partial_\mu$ and $\bar{\delta} = \bar{m}^\mu \partial_\mu$ are the directional derivatives. $\epsilon, \rho, \pi, \alpha, \beta, \tau, \mu$ and γ are the spin coefficients and the bar over the quantity denotes complex conjugation. The null tetrad basis vectors are choosen as

$$\begin{aligned} l^\mu &= \left\{ \left(1 - \kappa\eta^2 - \frac{2M}{r} - \frac{(1+L)\Lambda r^2}{3} \right)^{-1}, \frac{1}{\sqrt{1+L}}, 0, 0 \right\}, \\ n^\mu &= \left\{ \frac{1}{2}, \frac{-1}{2\sqrt{1+L}} \left(1 - \kappa\eta^2 - \frac{2M}{r} - \frac{(1+L)\Lambda r^2}{3} \right), 0, 0 \right\}, \\ m^\mu &= \left\{ 0, 0, \frac{1}{\sqrt{2}r}, \frac{i \csc \theta}{r\sqrt{2}} \right\}, \\ \bar{m}^\mu &= \left\{ 0, 0, \frac{1}{\sqrt{2}r}, \frac{i \csc \theta}{r\sqrt{2}} \right\}. \end{aligned} \quad (22)$$

The non-zero spin coefficients are found to be

$$\begin{aligned} \rho &= \frac{-1}{r\sqrt{1+L}}, \quad \mu = \frac{-1}{2r\sqrt{1+L}} \left(1 - \kappa\eta^2 - \frac{2M}{r} - \frac{(1+L)\Lambda r^2}{3} \right), \\ \gamma &= \frac{1}{4\sqrt{1+L}} \left(\frac{2M}{r^2} - \frac{2(1+L)\Lambda r}{3} \right), \quad \beta = \frac{\cot \theta}{2\sqrt{2}r}, \quad \alpha = -\frac{\cot \theta}{2\sqrt{2}r}. \end{aligned} \quad (23)$$

To decouple CDE (21) into radial and angular parts, we consider the spin-1/2 wave function in the form

$$\begin{aligned} B_1 &= R_1(r)A_1(\theta)e^{[i(\omega t + \bar{m}\phi)]}, \\ C_1 &= R_2(r)A_1(\theta)e^{[i(\omega t + \bar{m}\phi)]}, \\ B_2 &= R_2(r)A_2(\theta)e^{[i(\omega t + \bar{m}\phi)]}, \\ C_2 &= R_1(r)A_2(\theta)e^{[i(\omega t + \bar{m}\phi)]}, \end{aligned} \quad (24)$$

where ω is the frequency of the incoming Dirac field and m is the azimuthal quantum number of the wave. Substituting the spin coefficients (23) and the spinors (24) in Eq. (21), the radial and the angular parts are obtained as

$$\begin{aligned}
& \left[\frac{1}{\sqrt{1+L}} \left(1 + r \frac{d}{dr} \right) + i r \omega \left(1 - \kappa \eta^2 - \frac{2M}{r} - \frac{(1+L)\Lambda r^2}{3} \right)^{-1} \right] R_1 - i \mu^* r R_2 = -\lambda_1 R_2, \\
& \left[\frac{1}{\sqrt{1+L}} \left(1 - \kappa \eta^2 - \frac{2M}{r} - \frac{(1+L)\Lambda r^2}{3} \right) \left(1 + r \frac{d}{dr} \right) + \frac{r}{2\sqrt{1+L}} \left(\frac{2M}{r^2} - \frac{2(1+L)\Lambda r}{3} \right) - i r \omega \right] R_2 \\
& + 2i \mu^* r R_1 = \lambda_2 R_1, \\
& \left[\frac{1}{\sqrt{1+L}} \left(1 + r \frac{d}{dr} \right) + i r \omega \left(1 - \kappa \eta^2 - \frac{2M}{r} - \frac{(1+L)\Lambda r^2}{3} \right)^{-1} \right] R_1 - i \mu^* r R_2 = \lambda_3 R_2, \\
& \left[\frac{1}{\sqrt{1+L}} \left(1 - \kappa \eta^2 - \frac{2M}{r} - \frac{(1+L)\Lambda r^2}{3} \right) \left(1 + r \frac{d}{dr} \right) + \frac{r}{2\sqrt{1+L}} \left(\frac{2M}{r^2} - \frac{2(1+L)\Lambda r}{3} \right) - i r \omega \right] R_2 \\
& + 2i \mu^* r R_1 = -\lambda_4 R_1.
\end{aligned} \tag{25}$$

and

$$\begin{aligned}
\tilde{L}^+ A_2 &= \sqrt{2} A_1 \lambda_1, \quad \tilde{L}^- A_1 = \frac{1}{\sqrt{2}} A_2 \lambda_2, \\
\tilde{L}^- A_1 &= \sqrt{2} A_2 \lambda_3, \quad \tilde{L}^+ A_2 = \frac{1}{\sqrt{2}} A_1 \lambda_4,
\end{aligned} \tag{26}$$

where $\lambda_1, \lambda_2, \lambda_3$ and λ_4 are the separation constants. \tilde{L}^\pm are the angular operators, defined as

$$\tilde{L}^\pm = \frac{d}{d\theta} \pm \frac{\tilde{m}}{\sin \theta} + \frac{\cot \theta}{2}. \tag{27}$$

We take the separation constant as

$$\sqrt{2} \lambda_1 = \frac{1}{\sqrt{2}} \lambda_1 = -\lambda \quad \text{and} \quad \frac{1}{\sqrt{2}} \lambda_2 = \sqrt{2} \lambda_3 = \lambda. \tag{28}$$

Setting the eigenvalue $\lambda = -(l+1/2)$ for the angular equation, one can have the spin-weighted spheroidal harmonics [115, 116]. We carry out the following transformation to get the radial equations in the form of one-dimensional Schrödinger-like wave equations

$$R_1(r) = \frac{P_+(r)}{r}, \quad R_2(r) = \frac{1}{r} \left(1 - \kappa \eta^2 - \frac{2M}{r} - \frac{(1+L)\Lambda r^2}{3} \right)^{-\frac{1}{2}} P_-(r). \tag{29}$$

The radial equation becomes

$$\left(\frac{d}{dr_*} \pm i\omega \right) P_\pm = \sqrt{1 - \kappa \eta^2 - \frac{2M}{r} - \frac{(1+L)\Lambda r^2}{3}} \left(\frac{\lambda}{r} \pm i\mu_* \right) P_\mp, \tag{30}$$

where μ_* is the normalized rest mass of the spin-1/2 particle and r_* is the tortoise coordinate defined by

$$\frac{d}{dr_*} = \frac{1}{\sqrt{1+L}} \left(1 - \kappa \eta^2 - \frac{2M}{r} - \frac{(1+L)\Lambda r^2}{3} \right) \frac{d}{dr}, \tag{31}$$

3.3.1. Massless Dirac field perturbation

For massless Dirac field perturbation $\mu_* = 0$, and further letting

$$Z_\pm = P_- \pm P_+, \tag{32}$$

we obtain a pair of one dimensional Schrödinger-like wave equations

$$\left(\frac{d^2}{dr_*^2} + \omega^2\right)Z_{\pm} = V_{d\pm}Z_{\pm}, \quad (33)$$

where $V_{d\pm}$ are the effective potentials for the massless Dirac field :

$$V_{d\pm} = \frac{\left(l + \frac{1}{2}\right)^2}{r^2} \left(1 - \kappa\eta^2 - \frac{2M}{r} - \frac{(1+L)\Lambda r^2}{3}\right) \pm \left(l + \frac{1}{2}\right) \sqrt{1 - \kappa\eta^2 - \frac{2M}{r} - \frac{(1+L)\Lambda r^2}{3}} \times \frac{\{3M - r(1 - \kappa\eta^2)\}}{r^3 \sqrt{1+L}}. \quad (34)$$

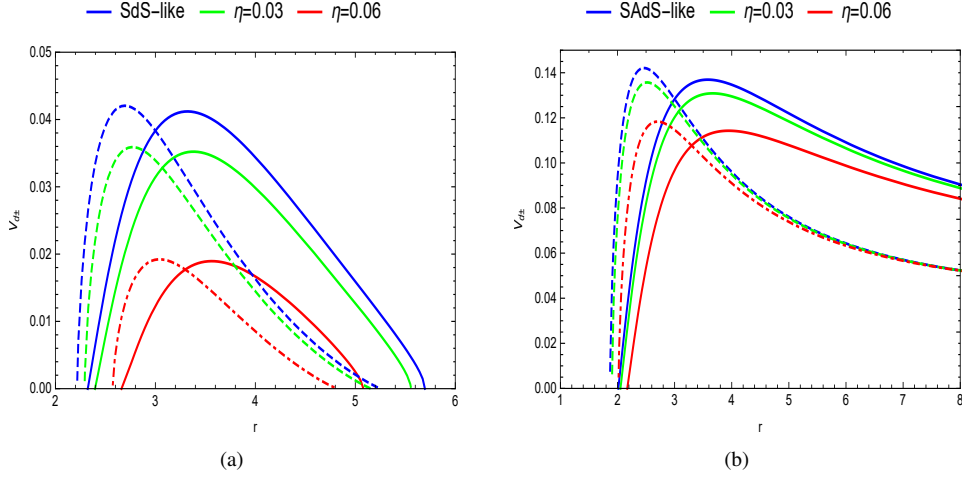


Figure 7: Graphs of the effective potential of the massless Dirac field perturbation: (a) SdS-like black hole ($\Lambda = 0.05$) and (b) SAdS-like black hole ($\Lambda = -0.05$) for different values of global monopole. The physical parameters are chosen as $M = 1$, $l = 1$ and $L = 0.2$.

The effect of global monopole parameter on the effective potential of massless Dirac field perturbation is illustrated in Fig. 7. The solid line represents V_{d+} , whereas the dashed line represents V_{d-} . Increasing the monopole parameter reduces the maximum of the effective potential in both the cases. This suggests that the monopole parameter increases the transmission of waves which tends to increase the greybody factor. It is also important to note that increasing the monopole parameter causes the maximum of the effective potential to occur at a larger radius for both dS and AdS cases. In Fig. 8, we highlight the role of Lorentz violation parameter in the effective potential of massless Dirac field perturbation. The Lorentz violation parameter L has opposite effect on the maximum of effective potential of massless Dirac field perturbation for dS and AdS cases. For dS case, increasing L reduces the maximum of the potential and the peak occurs at lower radius while for AdS case, the maximum of the potential increases and the peak occurs at larger radius. This signifies that as the value of L gets higher the greybody factor will be higher or lower according to the sign of Λ . The above remark will be thoroughly discussed in the subsequent section.

3.3.2. Massive Dirac field perturbation

Applying the transformation $Z = \tan^{-1}\left(\frac{\mu_* r}{\lambda}\right)$, Eq. (30) reduces to

$$\left(\frac{d}{dr_*} \pm i\omega\right)P_{\pm} = \sqrt{1 - \kappa\eta^2 - \frac{2M}{r} - \frac{(1+L)\Lambda r^2}{3}} \exp\left[\pm i \tan^{-1}\left(\frac{\mu_* r}{\lambda}\right)\right] \frac{(\lambda^2 + \mu_*^2 r^2)^{\frac{1}{2}}}{r} P_{\mp}. \quad (35)$$

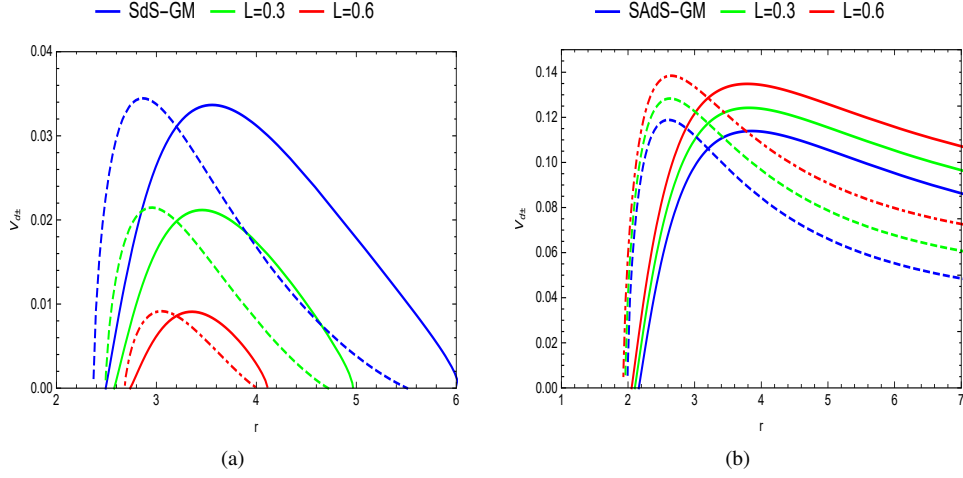


Figure 8: Graphs of the effective potential of the massless Dirac field perturbation: (a) SdS-like black hole ($\Lambda = 0.05$) and (b) SAdS-like black hole ($\Lambda = -0.05$) for different values of Lorentz violation parameter. The physical parameters are chosen as $M = 1$, $l = 1$ and $\eta = 0.05$.

Substituting $P_{\pm} = U_{\pm} \exp \left[\pm \frac{i}{2} \tan^{-1} \left(\frac{\mu_* r}{\lambda} \right) \right]$ and changing the variable r_* into \tilde{r}_* defined by

$$\tilde{r}_* = r_* + \frac{1}{2\omega} \tan^{-1} \left(\frac{\mu_* r}{\lambda} \right), \quad (36)$$

Eq. (35) reduces to

$$\left(\frac{d}{d\tilde{r}_*} \pm i\omega \right) U_{\pm} = W U_{\mp}, \quad (37)$$

where

$$W = \frac{\sqrt{1 - \kappa\eta^2 - \frac{2M}{r} - \frac{(1+L)\Lambda r^2}{3}} \sqrt{1+L} (\lambda^2 + r^2 \mu_*^2)^{\frac{3}{2}}}{r \left[\sqrt{1+L} (\lambda^2 + r^2 \mu_*^2) + \frac{\mu_* \lambda}{2\omega} \left(1 - \kappa\eta^2 - \frac{2M}{r} - \frac{(1+L)\Lambda r^2}{3} \right) \right]}. \quad (38)$$

Letting $\tilde{Z}_{\pm} = U_{-} \pm U_{+}$, we can readily obtain a pair of one dimensional Schrödinger-like wave equations

$$\left(\frac{d^2}{d\tilde{r}_*^2} + \omega^2 \right) \tilde{Z}_{\pm} = V_{dm\pm} \tilde{Z}_{\pm}, \quad (39)$$

where $V_{dm\pm}$ are the effective potentials of massive Dirac field perturbation given by

$$\begin{aligned} V_{dm\pm}(r) &= W^2 \pm \frac{dW}{d\tilde{r}_*} \\ &= \frac{\tilde{\Delta}^{\frac{1}{2}} \sqrt{1+L} \Xi^{\frac{3}{2}}}{\left[r^2 \sqrt{1+L} \Xi + \frac{\tilde{\Delta} \mu_* \lambda}{2\omega} \right]^2} + \left[\tilde{\Delta}^{\frac{1}{2}} \sqrt{1+L} \Xi^{\frac{3}{2}} \pm \left\{ 3r \tilde{\Delta} \mu_*^2 + \Xi \left(r - r\kappa\eta^2 - M - \frac{2\Lambda(1+L)r^3}{3} \right) \right\} \right] \\ &\mp \frac{\tilde{\Delta}^{\frac{3}{2}} \sqrt{1+L} \Xi^{\frac{5}{2}}}{\left[r^2 \sqrt{1+L} \Xi + \frac{\tilde{\Delta} \mu_* \lambda}{2\omega} \right]^3} \left[2r^3 \mu_*^2 \sqrt{1+L} + 2r \sqrt{1+L} \Xi + \frac{\mu_* \lambda}{\omega} \left(r - r\kappa\eta^2 - M - \frac{2\Lambda(1+L)r^3}{3} \right) \right], \end{aligned} \quad (40)$$

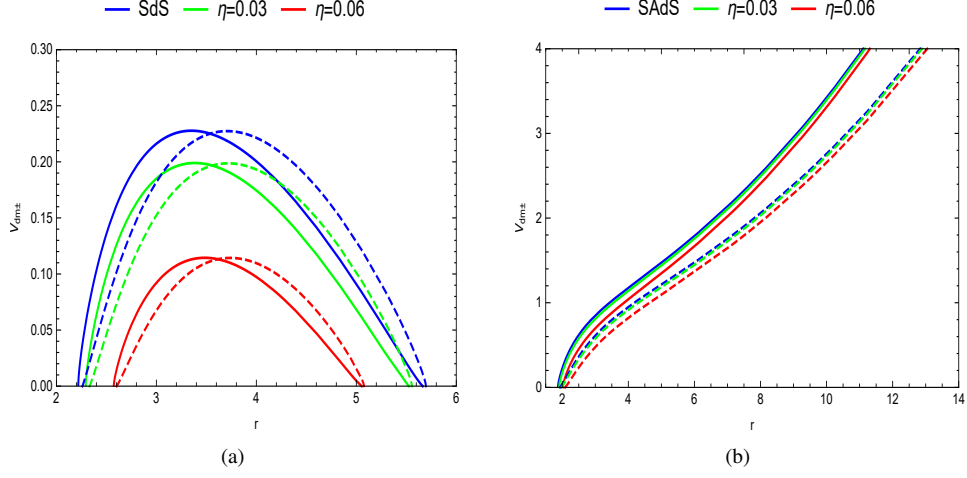


Figure 9: Graphs of the effective potential of the massive Dirac field perturbation: (a) SdS-like black hole ($\Lambda = 0.05$) and (b) SAdS-like black hole ($\Lambda = -0.05$) for different values of Lorentz violation parameter. The physical parameters are chosen as $M = 1$, $l = 1$ and $\eta = 0.05$.

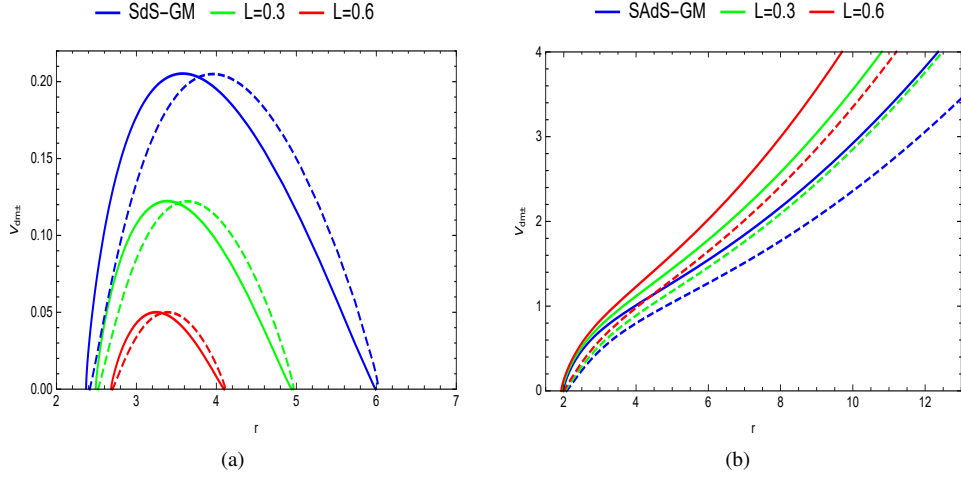


Figure 10: Graphs of the effective potential of the massive Dirac field perturbation: (a) SdS-like black hole ($\Lambda = 0.05$) and (b) SAdS-like black hole ($\Lambda = -0.05$) for different values of Lorentz violation parameter. The physical parameters are chosen as $M = 1$, $l = 1$ and $\eta = 0.05$.

where $\tilde{\Delta} = r^2 \left(1 - \kappa\eta^2 - \frac{2M}{r} - \frac{(1+L)\Lambda r^2}{3} \right)$ and $\Xi = (\lambda^2 + r^2\mu_*^2)$.

In Figs. 9 and 10, we illustrate the impact of Lorentz violation parameter and global monopole parameter on the effective potential of massive Dirac field perturbation. In both the dS and AdS cases, increasing the value of global monopole parameter lowers the peak of the effective potential thereby allowing the transmission of the waves more effectively. However, increasing the Lorentz violation parameter L lowers the peak of the effective potential in the dS case but it rises in the AdS case. For dS case, increasing the value of η shifts the peak of the effective potential towards the right but it shifts towards the left with increasing L .

4. Greybody factor

During the emission of black hole, some radiation is reflected back into the black hole and others are transmitted out of the black hole. This modifies the spectrum of Hawking radiation seen at spatial infinity [17]. The study of greybody factor is important in understanding the nature of the spectrum of Hawking radiation seen by an observer at a far distance from the event horizon of the black hole. In this section, we will study the rigorous bound of the greybody factor for scalar, electromagnetic and Dirac field perturbations. A rigorous bound of the transmission probability, which is the same as that of the greybody factor, is given by [24, 25]

$$T \geq \text{sech}^2 \left(\frac{1}{2\omega} \int_{-\infty}^{+\infty} |V_{eff}| dr_* \right). \quad (41)$$

For dS case, the presence of the event horizon and cosmological horizon provides a well defined setup of studying greybody factors based on wave scattering between two physical horizons. However, AdS spacetime features a time-like boundary at spatial infinity, which requires careful treatment of boundary conditions. Thus the study of greybody factor using rigorous bound technique in AdS is more subtle, so we restrict our analysis of greybody factor for dS case only.

For dS case, using the definition of r_* , the relation for bounds on greybody factors takes the following form

$$T \geq \text{sech}^2 \left(\frac{\sqrt{1+L}}{2\omega} \int_{r_h}^{r_c} \frac{|V_{eff}|}{f(r)} dr \right). \quad (42)$$

4.1. Scalar perturbation

Using Eqs. (2) and (11), in Eq. (42), we derive the expression for the rigorous bound of the greybody factor of scalar perturbation

$$T_s \geq \text{sech}^2 \left[\frac{\sqrt{1+L}}{2\omega} \left\{ l(1+l) \left(\frac{1}{r_c} - \frac{1}{r_e} \right) - \frac{2\Lambda(r_c - r_e)}{3(1+L)} - \frac{M}{(1+L)} \left(\frac{1}{r_c^2} - \frac{1}{r_e^2} \right) \right\} \right]. \quad (43)$$

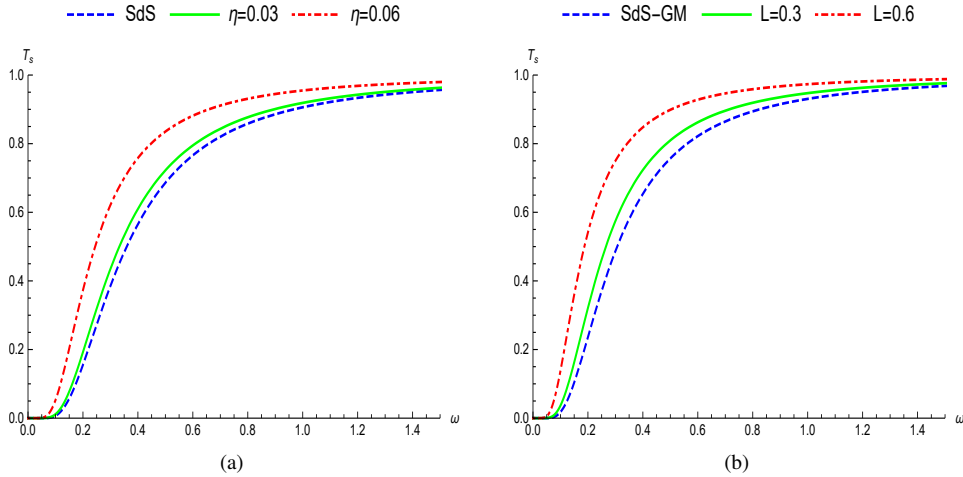


Figure 11: Graphs of the lower bound of the greybody factor of scalar field perturbation for different values of (a) global monopole parameter and (b) Lorentz violation parameter. The physical parameters are chosen as $M = 1$, $l = 1$ and $\Lambda = 0.05$.

From Eq. (43), one can readily see that the lower bound of the greybody factor of scalar perturbation depends on the Lorentz violation parameter. Further, the impact of the global monopole parameter can be determined by the

indication that the bound depends on the distance between the two horizons. We illustrate the variation of rigorous bound of the greybody factor for electromagnetic perturbation for different values of η and L in Figs. 11a and 11b respectively. One can observe that as the frequency increases, the lower bound on the greybody factor increases from zero to one. Moreover, increasing the Lorentz violation parameter and global monopole parameter increase the bound of greybody factor. It ultimately results in allowing more waves to reach a far distance observer.

4.2. Electromagnetic perturbation

Using the effective potential of electromagnetic perturbation (18), we derive the lower bound of the greybody factor

$$T_s \geq \text{sech}^2 \left[\frac{l(1+l)\sqrt{1+L}}{2\omega} \left(\frac{1}{r_e} - \frac{1}{r_c} \right) \right]. \quad (44)$$

Similar to the scalar perturbation, the lower bound of the greybody factor of the electromagnetic perturbation also depends on L and the distance between the horizons. Further, one can understand from Eq. (44) that if the distance between the horizons decrease, the angle in the RHS of (44) also decreases (for a clear point of view, we plot $r_c - r_a$ and $1/r_a - 1/r_c$ in Appendix A). Since RHS of (44) is a decreasing function for positive inputs, the lower bound of the greybody factor increases with decreasing the distance between the horizons. Moreover, we already obtained that the distance between the horizons are inversely proportional to η and L (see Figs. 1a and 2a). Thus, the rigorous bound of the greybody factor increases with increasing η and L . To analyse the effect of η and L numerically, we plot the rigorous bound of the greybody factor for different values of η and L in Figs. 12a and 12b respectively. The outcomes of the numerical analysis is also consistent with the earlier analysis.

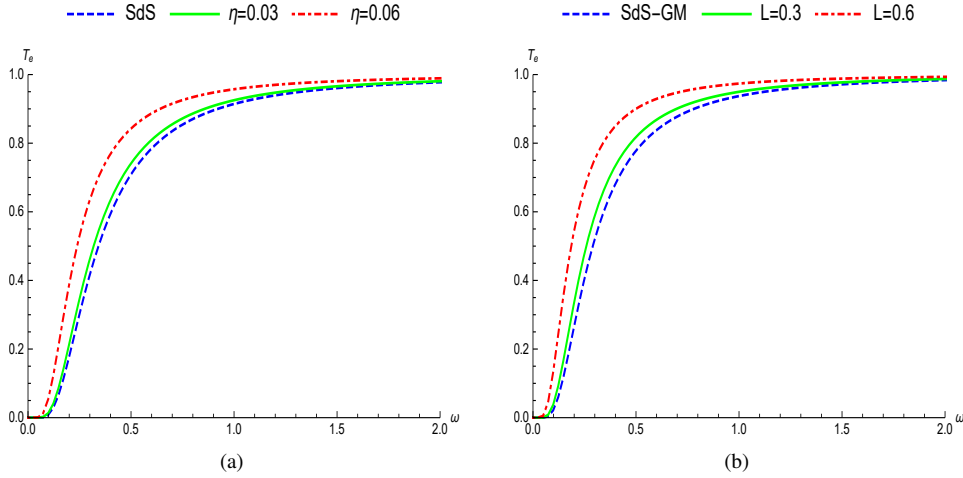


Figure 12: Graphs of the rigorous bound of the greybody factor of electromagnetic field perturbation for different values of (a) global monopole parameter and (b) Lorentz violation parameter. The physical parameters are chosen as $M = 1$, $l = 1$ and $\Lambda = 0.05$.

4.3. Massless Dirac perturbation

The lower bound of the greybody factor of massless Dirac perturbation is derived as

$$T_d \geq \text{sech}^2 \left[\frac{1}{2\omega} \left\{ -\sqrt{1+L} \left(l + \frac{1}{2} \right)^2 \left(\frac{1}{r_c} - \frac{1}{r_e} \right) \pm \left(l + \frac{1}{2} \right) \left(\frac{\sqrt{f(r_c)}}{r_c} - \frac{\sqrt{f(r_e)}}{r_e} \right) \right\} \right]. \quad (45)$$

Since $f(r)$ vanishes at the horizons, the lower bound of the greybody factor of massless Dirac perturbation reduces to

$$T_d \geq \text{sech}^2 \left[\frac{1}{2\omega} \left\{ \sqrt{1+L} \left(l + \frac{1}{2} \right)^2 \left(\frac{1}{r_e} - \frac{1}{r_c} \right) \right\} \right]. \quad (46)$$

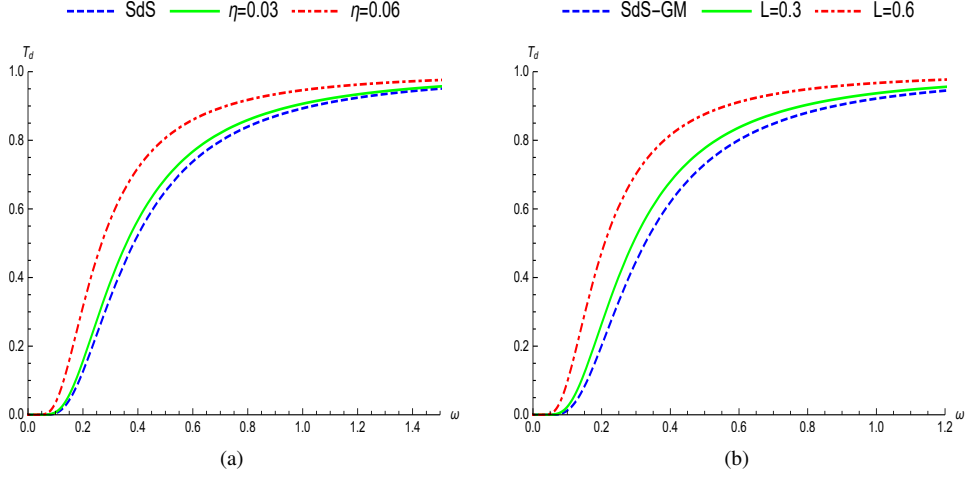


Figure 13: Graphs of the lower bound of the greybody factor of massless Dirac field perturbation for different values of (a) global monopole parameter and (b) Lorentz violation parameter. The physical parameters are chosen as $M = 1$, $l = 1$ and $\Lambda = 0.05$.

The lower bound of the greybody factor of massless Dirac perturbation is similar to that of electromagnetic perturbation. The lower bound of the greybody factor of massless Dirac perturbation for different values of η and L are depicted in Figs. 13a and 13b. Increasing the values of η and L increase the lower bound of the greybody factor thereby allowing more wave to be transmitted and reach a far distance observer.

4.4. Massive Dirac perturbation

The lower bound of the greybody factor of massive Dirac perturbation is derived as

$$T_{dm} = \text{sech}^2 \left[\frac{\sqrt{1+L}}{2\omega} \int_{r_e}^{r_c} A dr + \frac{1}{2\omega} \times W|_{r_e}^{r_c} \right], \quad (47)$$

where

$$A = \frac{\lambda^2(1+r^2\tilde{\mu}^2)}{r^2} \left[1 + \left(1 - \kappa\eta^2 - \frac{2M}{r} - \frac{(1+L)\Lambda r^2}{3} \right) \times \frac{\tilde{\mu}}{2\omega\sqrt{1+L}(1+r^2\tilde{\mu}^2)} \right]^{-1}, \quad \tilde{\mu} = \frac{\mu_*}{\lambda}. \quad (48)$$

It is noteworthy to mention that W vanishes at the horizon. Further, it is complicated to evaluate the full integral of Eq. (47), so we apply the approximation technique used in [26] and calculate the greybody factor bound as

$$\tilde{T}_d \geq \text{sech}^2 \left[\frac{\sqrt{1+L}}{2\omega} \left\{ \mu_*^2(r_c - r_h) - \lambda^2 \left(\frac{1}{r_c} - \frac{1}{r_e} \right) \right\} \right]. \quad (49)$$

In Fig. 14, we depicted the nature of rigorous bound of the greybody factor of massive Dirac field perturbation. In this case as well, the rigorous bound on the greybody factor rises as the parameters η and L increase implying that the resistance to the transmission of outgoing waves is reduced as the above parameters increase. It is evident that for every perturbation, the bounds asymptotically approach the value 1.

5. Quasinormal modes

In this section, we will calculate the QNM frequencies numerically, using the 6th order WKB approximation along with the improvements figured out using 6th order Padé Approximation. WKB method was first developed by

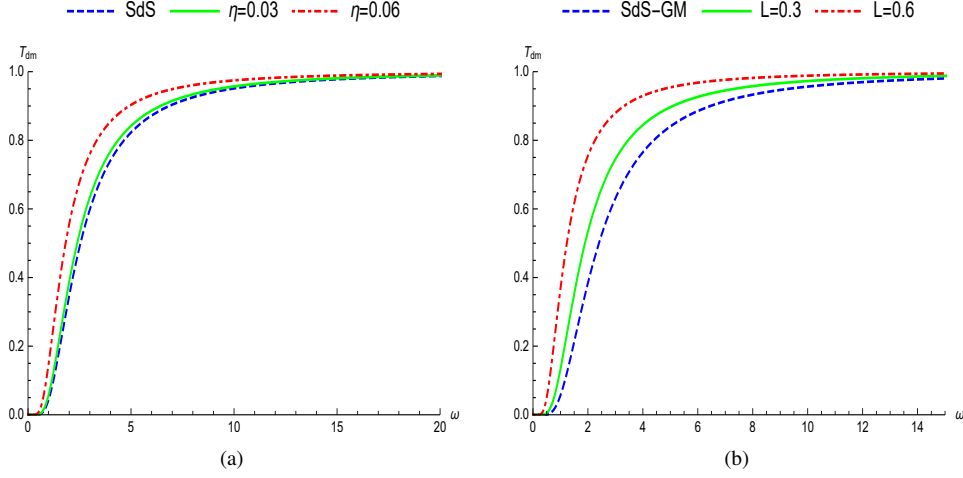


Figure 14: Graphs of the rigorous bound of the greybody factor of massive Dirac field perturbation for different values of (a) global monopole parameter and (b) Lorentz violation parameter. The physical parameters are chosen as $M = 1$, $l = 1$ and $\Lambda = 0.05$.

Schutz and Will [117] and extended to higher orders in Refs. [10, 118, 119]. The formula for calculating quasinormal frequencies using the 6th order WKB method is given by

$$\frac{i(\omega^2 - V(r_0))}{\sqrt{-2V''(r_0)}} - \Lambda_2 - \Lambda_3 - \Lambda_4 - \Lambda_5 - \Lambda_6 = n + \frac{1}{2}, \quad (50)$$

where $V(r_0)$ and $V''(r_0)$ represent the value of the potential and its second derivative with respect to the tortoise coordinate evaluated at its maxima r_0 . Here n denotes the overtone number. The expression of Λ_2 , Λ_3 , Λ_4 , Λ_5 , and Λ_6 can be found in [10, 118]. WKB method is reliable and accurate when the overtone number n is small compared to the multipole number l . However, when $n > l$ the method becomes less accurate. The precision of the WKB method can be enhanced by incorporating the Padé approximation technique introduced in [119, 120]. To obtain more accurate and reliable estimates for the QNM frequencies of the black hole in our work, we employ the Padé averaged 6th-order WKB approximation. Using the effective potentials of scalar, electromagnetic and Dirac perturbations, we compute the QNM frequencies and display in Table 1, 2 and 3 respectively.

In all the three types of perturbations, for a fixed multipole and overtone number, both the real part and the magnitude of the imaginary part of the QNM frequency decrease with increasing the Lorentz violation parameter L . This implies that the oscillation frequency and the damping rate decrease with increasing L . The same behaviours are obtained when η increases by fixing other parameters. Further, for fixed values of l , η and L , the real part of the quasinormal frequency decreases while the magnitude of imaginary part increases as n increase. Thus with increasing n , the oscillation frequency decreases but the damping rate increases. Further with increasing l and fixing other parameters, the oscillation frequency increases in all the perturbations. However, for varying l , the damping rate has different nature in different types of perturbation. With increasing l , the damping rate for scalar perturbation decreases but for electromagnetic perturbation it increases. For massless Dirac perturbation, the damping rate decreases in all the modes except for $n = 0$.

6. Shadow radius of black hole

In this section, we study the role of Lorentz violation parameter L and the monopole parameter η on the shadow radius of spherically symmetric black hole with global monopole in bumblebee gravity. For the metric (1), the Lagrangian is expressed as

$$2\mathcal{L} = f(r)\dot{t}^2 - \frac{(1+L)\dot{r}^2}{f(r)} - r^2\dot{\theta}^2 - r^2\sin^2\theta\dot{\varphi}^2, \quad (51)$$

Multipole Number	Overtone		WKB 6th Order	Padé Approximation
$\eta = 0.05, M = 1, \Lambda = 0.05$				
L				
$l = 1$	$n = 0$	0	0.166735 - 0.0608741 i	0.166727 - 0.0608164 i
		0.3	0.128337 - 0.0473977 i	0.128365 - 0.047382 I
		0.6	0.0834522 - 0.0300971 i	0.0827719 - 0.030395 i
$l = 2$	$n = 0$	0	0.288104 - 0.0581909 i	0.288104 - 0.0581887 i
		0.3	0.227598 - 0.0460515 i	0.227599 - 0.0460502 i
		0.6	0.14898 - 0.0300305 i	0.148821 - 0.0300655 i
$l = 2$	$n = 1$	0	0.28319 - 0.175442 i	0.28319 - 0.17544 i
		0.3	0.224701 - 0.138569 i	0.224729 - 0.138554 i
		0.6	0.149482 - 0.0892945 i	0.147912 - 0.0902552 i
$l = 3$	$n = 0$	0	0.407316 - 0.0575415 i	0.407316 - 0.0575413 i
		0.3	0.323613 - 0.0457497 i	0.323613 - 0.0457495 i
		0.6	0.212272 - 0.0299885 i	0.212282 - 0.0299877 i
$l = 3$	$n = 1$	0	0.403528 - 0.173022 i	0.403528 - 0.173022 i
		0.3	0.32156 - 0.137403 i	0.321564 - 0.137403 i
		0.6	0.211545 - 0.090035 i	0.21167 - 0.0899829 i
$l = 3$	$n = 2$	0	0.396106 - 0.289701 i	0.396106 - 0.289701 i
		0.3	0.317454 - 0.229547 i	0.317461 - 0.22953 i
		0.6	0.209785 - 0.150508 i	0.210437 - 0.150045 i
$L = 0.2, M = 1, \Lambda = 0.05$				
η				
$l = 1$	$n = 0$	0	0.182786 - 0.0692195 i	0.182778 - 0.0691352 i
		0.03	0.16827 - 0.0631862 i	0.168271 - 0.0631013 i
		0.06	0.121599 - 0.0442161 i	0.121644 - 0.0442013 i
$l = 2$	$n = 0$	0	0.3186195 - 0.0665137 i	0.3186198 - 0.0665106 i
		0.03	0.2943335 - 0.0607819 i	0.2943338 - 0.0607794 i
		0.06	0.2151813 - 0.0428825 i	0.2151812 - 0.0428824 i
$l = 2$	$n = 1$	0	0.312616 - 0.200608 i	0.312614 - 0.200606 i
		0.03	0.289238 - 0.183226 i	0.289236 - 0.18322 i
		0.06	0.212602 - 0.129005 i	0.212602 - 0.129005 i
$l = 3$	$n = 0$	0	0.451375 - 0.0658817 i	0.451375 - 0.0658814 i
		0.03	0.417276 - 0.0602284 i	0.417276 - 0.0602281 i
		0.06	0.3057934 - 0.0425843 i	0.3057935 - 0.0425841 i
$l = 3$	$n = 1$	0	0.4467949 - 0.198135 i	0.4467948 - 0.198134 i
		0.03	0.4134373 - 0.181071 i	0.4134372 - 0.18107 i
		0.06	0.303949 - 0.12789 i	0.303957 - 0.127889 i
$l = 3$	$n = 2$	0	0.4378079 - 0.331875 i	0.4378075 - 0.331874 i
		0.03	0.405877 - 0.303093 i	0.405876 - 0.303091 i
		0.06	0.300251 - 0.213639 i	0.300281 - 0.213602 i

Table 1: QNM frequencies for scalar perturbation for the SdS-like black hole with global monopole calculated using 6th order WKB and 6th order Padé Approximation for different modes and for different values of the Lorentz violation parameter and monopole parameter.

Multipole Number	Overtone		WKB 6th Order	Padé Approximation
$\eta = 0.05, M = 1, \Lambda = 0.05$				
		L		
$l = 1$	$n = 0$	0	0.154693 - 0.0557613 i	0.154695 - 0.0557307 i
		0.3	0.124014 - 0.0448676 i	0.124022 - 0.0448217 i
		0.6	0.0799587 - 0.030461 i	0.0819019 - 0.0297455 i
$l = 2$	$n = 0$	0	0.281284 - 0.0565098 i	0.281284 - 0.0565086 i
		0.3	0.2249958 - 0.0452443 i	0.2249957 - 0.0452439 i
		0.6	0.148313 - 0.0298338 i	0.148241 - 0.0298501 i
$l = 2$	$n = 1$	0	0.275597 - 0.170178 i	0.275596 - 0.170178 i
		0.3	0.2221306 - 0.135928 i	0.2221308 - 0.135932 i
		0.6	0.148154 - 0.0891358 i	0.14744 - 0.0895641 i
$l = 3$	$n = 0$	0	0.402504 - 0.0567037 i	0.402504 - 0.0567036 i
		0.3	0.321751 - 0.0453484 i	0.321751 - 0.0453483 i
		0.6	0.211872 - 0.029877 i	0.211859 - 0.0298794 i
$l = 3$	$n = 1$	0	0.398492 - 0.1704388 i	0.398492 - 0.1704387 i
		0.3	0.319716 - 0.136148 i	0.319716 - 0.136149 i
		0.6	0.211429 - 0.0895877 i	0.211285 - 0.089648 i
$l = 3$	$n = 2$	0	0.390427 - 0.285232 i	0.390438 - 0.285227 i
		0.3	0.315603 - 0.227278 i	0.315603 - 0.227279 i
		0.6	0.210875 - 0.148929 i	0.210125 - 0.149455 i
$L = 0.2, M = 1, \Lambda = 0.05$				
		η		
$l = 1$	$n = 0$	0	0.170869 - 0.0638577 i	0.170874 - 0.0638116 i
		0.03	0.15851 - 0.0585237 i	0.158513 - 0.0584857 i
		0.06	0.117419 - 0.0417628 i	0.117419 - 0.0417425 i
$l = 2$	$n = 0$	0	0.311815 - 0.0647804 i	0.311815 - 0.0647786 i
		0.03	0.288715 - 0.0592863 i	0.288715 - 0.0592853 i
		0.06	0.21265 - 0.0421061 i	0.21265 - 0.0421056 i
$l = 2$	$n = 1$	0	0.304972 - 0.195159 i	0.304973 - 0.195158 i
		0.03	0.283058 - 0.178463 i	0.283059 - 0.178464 i
		0.06	0.210086 - 0.126487 i	0.210086 - 0.126488 i
$l = 3$	$n = 0$	0	0.446564 - 0.0650204 i	0.446564 - 0.0650202 i
		0.03	0.413295 - 0.0594857 i	0.413295 - 0.0594856 i
		0.06	0.303987 - 0.0421981 i	0.303987 - 0.042198 i
$l = 3$	$n = 1$	0	0.441738 - 0.195474 i	0.441738 - 0.195474 i
		0.03	0.4093 - 0.178765 i	0.4093 - 0.178765 i
		0.06	0.302167 - 0.126683 i	0.302167 - 0.126683 i
$l = 3$	$n = 2$	0	0.432041 - 0.327268 i	0.432057 - 0.327259 i
		0.03	0.401254 - 0.299042 i	0.40126 - 0.299042 i
		0.06	0.298487 - 0.211453 i	0.298487 - 0.211453 i

Table 2: QNM frequencies for electromagnetic perturbation for the SdS-like black hole with global monopole calculated using 6th order WKB and 6th order Padé Approximation for different modes and for different values of the Lorentz violation parameter and monopole parameter.

Multipole Number	Overtone		WKB 6th Order	Padé Approximation
$\eta = 0.05, M = 1, \Lambda = 0.05$				
		L		
$l = 1$	$n = 0$	0	0.174652 - 0.0567557 i	0.17465 - 0.0567437 i
		0.3	0.139148 - 0.0451919 i	0.138581 - 0.0453736 i
		0.6	0.125657 - 0.0228762 i	0.0908757 - 0.0299374 i
$l = 2$	$n = 0$	0	0.292869 - 0.0568447 i	0.292868 - 0.0568451 i
		0.3	0.233379 - 0.0453983 i	0.233328 - 0.0454091 i
		0.6	0.151933 - 0.0303426 i	0.153298 - 0.0298997 i
$l = 2$	$n = 1$	0	0.287301 - 0.171186 i	0.287294 - 0.171195 i
		0.3	0.231081 - 0.136086 i	0.230861 - 0.136485 i
		0.6	0.140511 - 0.0994076 i	0.152387 - 0.0898092 i
$l = 3$	$n = 0$	0	0.410708 - 0.0568714 i	0.327625 - 0.0454266 i
		0.3	0.327608 - 0.0454285 i	0.327625 - 0.0454266 i
		0.6	0.218379 - 0.029537 i	0.21543 - 0.0299024 i
$l = 3$	$n = 1$	0	0.406732 - 0.170944 i	0.406732 - 0.170945 i
		0.3	0.325417 - 0.136461 i	0.325604 - 0.136383 i
		0.6	0.247312 - 0.078325 i	0.214863 - 0.0897147 i
$l = 3$	$n = 2$	0	0.398756 - 0.286073 i	0.39876 - 0.286074 i
		0.3	0.320559 - 0.228353 i	0.321528 - 0.227676 i
		0.6	0.376022 - 0.0863962 i	0.213723 - 0.149558 i
$L = 0.2, M = 1, \Lambda = 0.05$				
		η		
$l = 1$	$n = 0$	0	0.192324 - 0.0650849 i	0.192317 - 0.0650785 i
		0.03	0.17813 - 0.0595326 i	0.178126 - 0.0595232 i
		0.06	0.130443 - 0.0425033 i	0.131332 - 0.0422138 i
$l = 2$	$n = 0$	0	0.32414 - 0.0651743 i	0.324138 - 0.0651765 i
		0.03	0.299988 - 0.0596109 i	0.299987 - 0.0596111 i
		0.06	0.220719 - 0.04224 i	0.220657 - 0.0422537 i
$l = 2$	$n = 1$	0	0.3175 - 0.196308 i	0.317449 - 0.196347 i
		0.03	0.294452 - 0.179434 i	0.294447 - 0.179443 i
		0.06	0.218732 - 0.126573 i	0.218124 - 0.12693 i
$l = 3$	$n = 0$	0	0.455254 - 0.0652122 i	0.455254 - 0.0652119 i
		0.03	0.42125 - 0.0596431 i	0.421249 - 0.0596435 i
		0.06	0.309644 - 0.0422681 i	0.309639 - 0.0422692 i
$l = 3$	$n = 1$	0	0.450474 - 0.1960514 i	0.450475 - 0.1960511 i
		0.03	0.417304 - 0.179233 i	0.417292 - 0.179241 i
		0.06	0.307895 - 0.12687 i	0.307867 - 0.126895 i
$l = 3$	$n = 2$	0	0.440867 - 0.328238 i	0.440892 - 0.328225 i
		0.03	0.409391 - 0.29978 i	0.409377 - 0.299805 i
		0.06	0.304512 - 0.211582 i	0.304183 - 0.211814 i

Table 3: QNM frequencies for massless Dirac perturbation for the SdS-like black hole with global monopole calculated using 6th order WKB and 6th order Padé Approximation for different modes and for different values of the Lorentz violation parameter and monopole parameter.

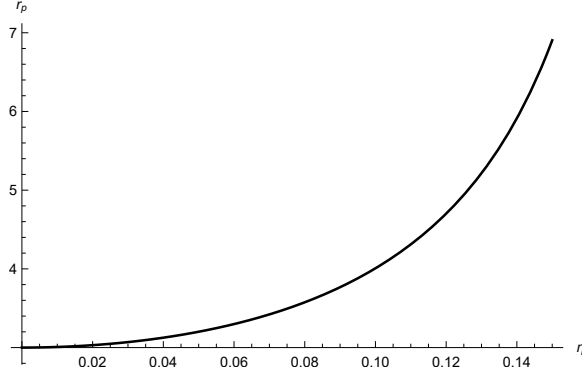


Figure 15: Plot of photon radius for different values of η and fixed $M = 1$.

where the overdot symbol represents the derivative with respect to the proper time τ . Without loss of generality, we restrict our analysis only to the equatorial plane i.e. $\theta = \frac{\pi}{2}$. The generalized momenta are derived from the Lagrangian (51) as

$$p_t = f(r)\dot{t} = E, \quad p_r = \frac{1+L}{f(r)}\dot{r}, \quad p_\phi = -r^2\dot{\phi} = -\mathcal{L}, \quad (52)$$

where E and \mathcal{L} are the energy and angular momentum of the particle. Using Eq. (52), Eq. (51) for null geodesic can be written as

$$\dot{r}^2 + V = 0, \quad (53)$$

where

$$V = \frac{1}{1+L} \left(\frac{f(r)\mathcal{L}^2}{r^2} - E^2 \right). \quad (54)$$

The null-like geodesics of the equatorial circular motion should satisfy the conditions

$$V(r)|_{r=r_p} = 0 \quad \text{and} \quad V'(r)|_{r=r_p} = 0, \quad (55)$$

where r_p is the radius of the photon sphere. The critical impact parameter for the photon sphere is

$$b_c = \frac{\mathcal{L}}{E} = \frac{r_p}{\sqrt{f(r_p)}}. \quad (56)$$

From Eq. (55), one can obtain the radius of the photon sphere as

$$r_p = \frac{3M}{(1 - \kappa\eta^2)}. \quad (57)$$

From the expression of r_p , one can observe that the monopole parameter has a significant impact on the radius of the photon sphere. However, the Lorentz violation does not affect it. The photon radius is illustrated in Fig. 15. Further, the radius of the black hole shadow observed from a distant static observer at the position r_0 [121] is found to be

$$\mathcal{R}_s = r_p \sqrt{\frac{f(r_0)}{f(r_p)}}. \quad (58)$$

Assuming the observer is sufficiently far away from the black hole, we can consider $f(r_0) \approx 1$. Thus the shadow radius reduces to

$$\mathcal{R}_s = \frac{r_p}{\sqrt{f(r_p)}}. \quad (59)$$

Further, the shadow radius can also be represented by the celestial coordinate (X, Y) as

$$\mathcal{R}_s = \sqrt{X^2 + Y^2}, \quad (60)$$

where $X = \lim_{r_0 \rightarrow \infty} (-r_0^2 \sin \theta_0 \frac{d\phi}{dr}|_{r_0, \theta_0})$ and $Y = \lim_{r_0 \rightarrow \infty} (r_0^2 \frac{d\theta}{dr}|_{r_0, \theta_0})$. Here (r_0, θ_0) denotes the positions of the observer at spatial infinity. For equatorial plane, the shadow radius is equivalent to the critical impact parameter of the photon sphere. Thus the shadow radius is expressed as

$$\mathcal{R}_s = \frac{r_p}{\sqrt{1 - \kappa\eta^2 - \frac{2M}{r_p} - \frac{(1+L)\Lambda r_p^2}{3}}}. \quad (61)$$

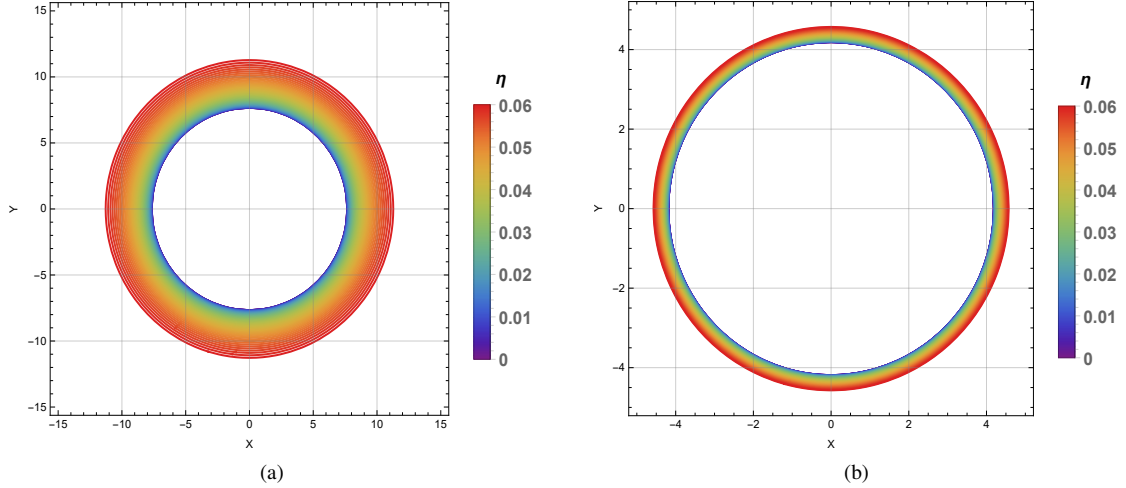


Figure 16: Plot of the shadow radius of (a) SAdS-like black hole with global monopole (b) SdS-like black hole with global monopole for different values of global monopole parameter with fixed $L = 0.2$, $M = 1$ and $\Lambda = 0.05$.

To analyse the qualitative nature of variation of black hole shadow radius, we plot \mathcal{R}_s for different values of η and L in Figs. 16 and 17 respectively. It is observed that shadow radius increases with increasing the parameters η for both the dS and AdS cases. However with increasing the Lorentz violation parameter, the shadow radius may increase or decrease according to dS or AdS case. The effects of Lorentz violation parameter and monopole parameter on the photon radius and shadow radius of dS and AdS spacetimes are shown in tables 4 and 5 respectively. For fixed L , both r_p and \mathcal{R}_s increase with increasing η . However for fixed η , r_p remains constant and \mathcal{R}_s increases with increasing L . It

η	0	0.03	0.06	0.08	0.05	0.05	0.05	0.05
L	0.2	0.2	0.2	0.2	0	0.3	0.6	0.8
r_p	3	3.06943	3.29844	3.57504	3.20113	3.20113	3.20113	3.20113
\mathcal{R}_s	7.66131	8.28168	11.2751	23.0298	8.50686	10.6488	16.1828	45.3991

Table 4: Various values of photon radius and shadow radius for different values of η and L with fixed $M=1$ and $\Lambda = 0.05$.

is worth mentioning that measurements of the shadow size around the black hole may help to estimate the black hole parameters and also probe the geometry of the background metric.

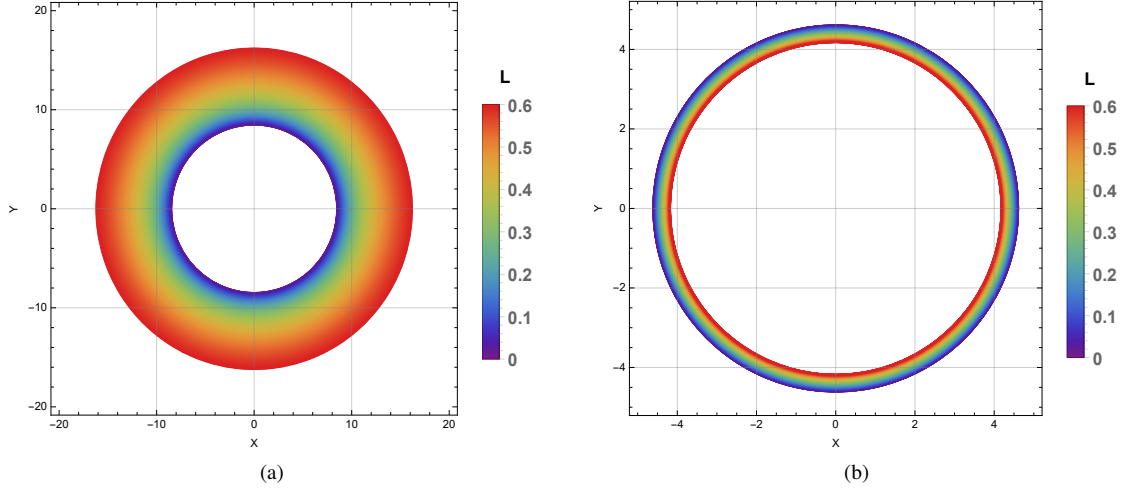


Figure 17: Plot of the shadow radius of (a) SdS-like black hole with global monopole (b) SAdS-like black hole with global monopole for different values of Lorentz violation parameter L with fixed $\eta = 0.05$, $M = 1$ and $\Lambda = 0.05$.

η	0	0.03	0.06	0.08	0.05	0.05	0.05	0.05
L	0.2	0.2	0.2	0.2	0	0.3	0.6	0.8
r_p	3	3.06943	3.29844	3.57504	3.20113	3.20113	3.20113	3.20113
R_s	4.18718	4.28038	4.57073	4.88617	4.60522	4.3789	4.18297	4.06608

Table 5: Various values of photon radius and shadow radius for different values of η and L with fixed $M=1$ and $\Lambda = -0.05$.

7. High-energy absorption cross-section

The study of absorption cross-section of a black hole is one of the interesting aspects in investigating the field perturbation around the black hole. The absorption cross-section of a black hole is the measure of how much the incoming particles is absorbed by the black hole rather than dispersed. In this section, we calculate the high-energy absorption cross-section using the sinc approximation method. Sanchez [122] proposed that in the high-frequency regime, the total absorption cross-section oscillated around the constant geometric-optics value for the black hole. For low-energy regime, the absorption cross-section is equal to the area of black hole at the horizon [123]. Further, Decanini et al. [124] used the Regge pole techniques to prove the oscillatory part of the absorption cross-section in the high-frequency regime is related to a sinc(x) function including the photon sphere. In the sinc approximation, the oscillatory part of the absorption cross-section is given by

$$\sigma_{osc} = -8\pi\sigma_{geo} n_c \exp[-\pi n_c] \text{sinc} \left[\frac{2\pi\omega}{\Omega_c} \right], \quad (62)$$

where $\text{sinc } z = \sin z/z$ is the sine cardinal, $\sigma_{geo} = \pi b_c^2$ is the geometrical absorption cross-section, $\Omega_p = \sqrt{\frac{f_p}{r_p}}$ is the orbital angular velocity, r_p is the radius of the unstable null circular orbit and n_c is a factor related to the Lyapunov exponent λ_p at the unstable circular orbits radius [125]

$$n_c = \frac{\lambda_p}{\Omega_p}. \quad (63)$$

The Lyapunov exponent is given by the relation

$$\lambda_p = \sqrt{-\frac{V'''}{2\dot{t}^2}}. \quad (64)$$

Using Eq. (54), we derived the expression as

$$\lambda_p = \frac{f(r_p)}{2(1+L)r_p^2} \left[2f(r_p) - r_p^2 f''(r_p) \right] \\ = \frac{(1 - \kappa\eta^2)(1 - 3\kappa\eta^2 + 3\kappa^2\eta^4 - \kappa^3\eta^6 - 9(1+L)M^2\Lambda)}{27(1+L)M^2}. \quad (65)$$

Then the total absorption cross-section in the limit for high frequencies using sinc approximation is given by

$$\sigma_{abs} \approx \sigma_{osc} + \sigma_{geo}. \quad (66)$$

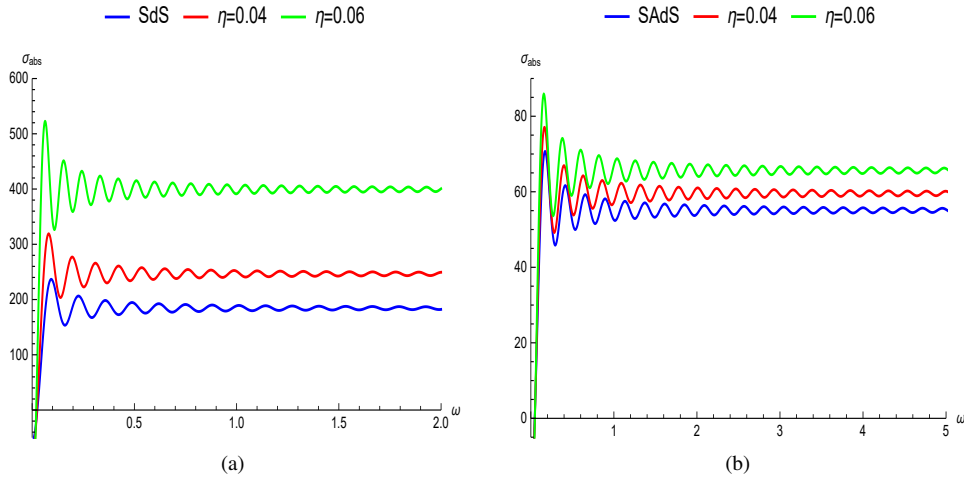


Figure 18: Graphs of the total absorption cross-section for different values of η .

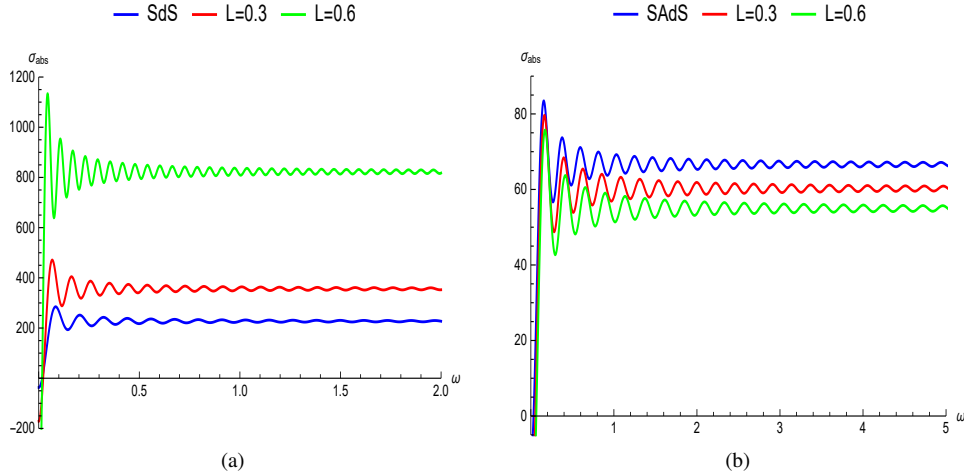


Figure 19: Graphs of the total absorption cross-section for different values of L with fixed $M = 1$.

We plot the total absorption cross-section for various values of η and L in Figs. 18 and 19 respectively. In all the graphs, we observe the three stages of absorption cross-section: (i) the fast growing phase at low frequency, (ii) the

intermediate oscillating phase which is a characteristic of interference due to potential barriers and (iii) finally at high frequency the cross section starts to level off. With increasing the monopole parameter, the absorption cross-section becomes higher in both the dS and AdS cases. The absorption cross-section will increase with increasing L in dS case but it will be an opposite effect in AdS black hole.

8. Conclusion

In this work, we investigated scalar, electromagnetic and Dirac perturbations of SdS/AdS-like black hole with a global monopole in bumblebee gravity. We analysed the effective potentials of the above three perturbations and studied the effects of η and L in the effective potential, greybody factors, QNMs, shadow radius and absorption cross-section of the black hole. In the region between the event horizon and cosmological horizon, the nature of effective potentials are same for all the perturbations. For both dS and AdS cases, increasing the η leads to a lower potential barrier. However the L has an opposite effects on the effective potential in dS and AdS backgrounds. Increasing L lowers the potential barrier in the dS case but it has an opposite effect in AdS case. Our analysis of greybody factor is limited to the dS only. The greybody factor is analysed using the rigorous bound technique. In all the perturbations, we found that the lower bounds of the greybody factor increases with increasing L and η . Thus, increasing the η and L facilitate the ability of waves to propagate through the black hole potential and reach asymptotic observers. This behaviour is consistent with the fact that higher values of L and η correspond to the lower potential making it easier for waves to transmit through the barrier.

We also derived numerically, the QNMs of dS case by applying the 6th order WKB method and Padé method for varying η and L . Increasing the parameters L and η reduce both the oscillation frequency and the decay rate. For any value of L and η , we found no modes with positive damping in all the perturbations. This indicates the stability of SdS black hole perturbation in the presence of global monopole and Lorentz violation. The photon sphere radius and black hole shadow radius are also discussed. Our analysis reveals that with increasing η , the photon sphere expands and an enlarged black hole shadow is found for both dS and AdS spacetimes. It is noted that increasing the value of L prevents the rise of shadow radius in AdS black hole but it has an opposite effect for dS black hole. We also examine the absorption cross-section of the black hole and find that it rises with increasing values of η for both dS and AdS black holes. However, the role of L again differs between the two spacetimes. Higher L reduces the absorption cross-section in AdS spacetime but it increases the cross-section in a dS background.

Our analysis will enhance the understanding of how the global monopole parameter and Lorentz violation theory influence black hole observables such as QNM frequencies, shadow profile and thermal radiation properties of black holes. This will contribute to a deeper theoretical understanding of modified gravity scenarios and provide insight into how topological defects and Lorentz-violating effect the future gravitational wave signals and black hole imaging data. The present work excludes the study of gravitational lensing and time-domain analysis of QNMs, which are crucial for a more complete understanding of black hole dynamics and observational signatures. We intend to investigate these in near future.

Appendix A

From Fig. 20, one can see that both $r_c - r_e$ and $\frac{1}{r_e} - \frac{1}{r_c}$ are strictly positive and decreasing with increasing η and L . This confirms that the angle in RHS of (44) is positive and it decreases with decreasing the horizon distance.

References

- [1] H.W. Press, *Astrophys. J.* 170 (1971) L105.
- [2] S.L. Detweiler, *Astrophys. J.* 239 (1980) 292.
- [3] V.C. Vishveshwara, *Nature* 227 (1970) 936.
- [4] H.P. Nollert, *Class. Quantum Gravity* 16 (1999) R159.
- [5] E. Berti, V. Cardoso, A.O. Starinets, *Class. Quantum Gravity* 26 (2009) 163001.
- [6] K. Akiyama, et al., Event Horizon Telescope, *Astrophys. J. Lett.* 930 (2022) L17.
- [7] C. Goddi, et al., *Int. J. Mod. Phys. D* 26 (2016) 1730001.
- [8] B.F. Schutz, C.M. Will, *Astrophys. J.* 291 (1985) L33.
- [9] S. Iyer, *Phys. Rev. D* 35 (1987) 3632.

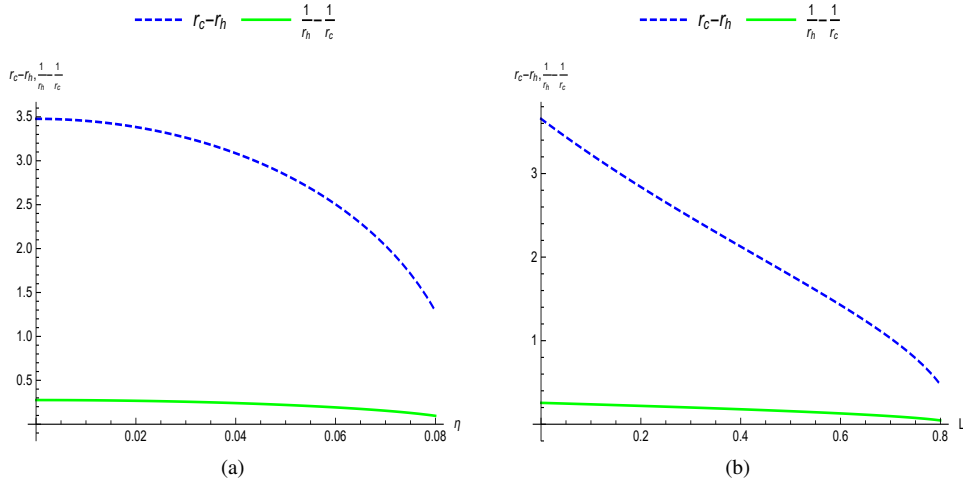


Figure 20: Graphs illustrating the behavior of $r_c - r_h$ and $\frac{1}{r_h} - \frac{1}{r_c}$ versus η and L respectively.

- [10] S. Iyer, C.M. Will, Phys. Rev. D 35 (1987) 3621.
- [11] W. Wahlang, P.A. Jeena, S. Chakrabarti, Int. J. Mod. Phys. D 26 (2017) 1750160.
- [12] S. Chandrasekhar, Fundam. Theor. Phys. 9 (1984) 5.
- [13] A. Övgün, İ Sakallı, J. Saavedra, Chin. Phys. C 42 (2018) 105102.
- [14] R.A. Konoplya, A. Zhidenko, Rev. Mod. Phys. 83 (2011) 793.
- [15] E.W. Leaver, Proc. R. Soc. Lond. A 402 (1985) 285.
- [16] H.-J. Blome, B. Mashhoon, Phys. Lett. A 100 (1984) 231.
- [17] S.W. Hawking Commun. Math. Phys. 43 (1975) 199.
- [18] D. Singleton, S. Wilburn, Phys. Rev. Lett. 107 (2011) 081102.
- [19] M. Cvetič, F. Larsen, Phys. Rev. D 56 (1997) 4994.
- [20] S. Fernando, Gen. Relativ. Gravit. 37 (2005) 461
- [21] W. Kim, J.Korean Phys. Soc. 52 (2008) 986
- [22] M.K. Parikh, F. Wilczek, Phys. Rev. Lett. 85 (2000) 5042
- [23] R.A. Konoplya, A.F. Zinhailo, Phys. Lett. B 810 (2020) 135793
- [24] M. Visser, Phys. Rev. A 59 (1999) 427.
- [25] P. Boonserm, M. Visser, Ann. Phys. 323 (2008) 2779.
- [26] P. Boonserm, C. H. Chen, T. Ngampitipan, P. Wongjun, Phys. Rev. D 104 (2021) 084054.
- [27] P. Boonserm, T. Ngampitipan, M. Visser, J. High Energy Phys. 03 (2014) 113.
- [28] R. Konoplya, A. Zhidenko, Phys. Lett. B 756 (2016) 350.
- [29] G.T. Zatspein, V.A. Kuzmin, JETP Lett. 4 (1966) 78.
- [30] M. Takeda, et al., Phys. Rev. Lett. 81 (1998) 1163.
- [31] V.A. Kostelecky, S. Samuel, Phys. Rev. Lett. 66 (1991) 1811.
- [32] S. Coleman, S.L. Glashow, Phys. Rev. D 59 (1999) 116008.
- [33] S.T. Scully, F.W. Stecker, Astroparticle Phys. 31 (2009) 220.
- [34] V.A. Kostelecky, M. Mewes, Phys. Rev. Lett. 87 (2001) 251304.
- [35] V.A. Kostelecky, M. Mewes, Phys. Rev. D 66 (2002) 056005 .
- [36] R. Bluhm, V.A. Kostelecky, C.D. Lane, Phys. Rev. Lett. 84 (2000) 1098 .
- [37] V.W. Hughes et al., Phys. Rev. Lett. 87 (2001) 111804.
- [38] V.A. Kostelecky, Phys. Rev. Lett. 80 (1998) 1818 .
- [39] V.A. Kostelecky, Phys. Rev. D 61 (2000) 016002 .
- [40] V.A. Kostelecky, Phys. Rev. D 64 (2001) 076001.
- [41] V.A. Kostelecky, C.D. Lane, Phys. Rev. D 60 (1999) 116010.
- [42] D. Bear et al., Phys. Rev. Lett. 85 (2000) 5038.
- [43] D. Colladay, P. McDonald, Phys. Rev. D 75 (2007) 105002.
- [44] R. Jackiw, V.A. Kostelecky, Phys. Rev. Lett. 82 (1999) 3572.
- [45] V.A. Kostelecky, S. Samuel, Phys. Rev. Lett. 63 (1989) 224.
- [46] N. Media, S. Christina, T.S. Ibungochouba, Int. J. Mod. Phys. A 39 (2024) 2450105.
- [47] Y.L. Onika, T.S. Ibungochouba, I.M. Ablu, Gen. Relativ. Gravit. 54 (2022) 77.
- [48] Y.S. Priyobarta, T.S. Ibungochouba, I.M. Ablu, A. S. Keshwarjit, Int. J. Mod. Phys. D 31 (2022) 2250106.
- [49] N. Media, Y.L. Onika, T.S. Ibungochouba, Int. J. Geom. Methods Mod. Phys. 20 (2023) 2350217.

- [50] Y.S. Priyobarta, T.S. Ibungochouba, S.S. Niranjana, Chin. Phys. C 48 (2024) 115111.
- [51] Y.L. Onika, T.S. Ibungochouba, I.M. Ablu, Mod. Phys. Lett. A 38 (2023) 2350089.
- [52] V.A. Kostelecky, S. Samuel, Phys. Rev. D 40 (1989) 1886.
- [53] R.V. Maluf, J.C.S. Neves, Phys. Rev. D 103 (2021) 044002.
- [54] V.A. Kostelecky, S. Samuel, Phys. Rev. D 39 (1989) 683.
- [55] A.V. Kostelecky, J.D. Tasson, Phys. Rev. D 83 (2011) 016013 .
- [56] Q.G. Bailey, V.A. Kostelecky, Phys. Rev. D 74 (2006) 045001.
- [57] R.V. Maluf, V. Santos, W.T. Cruz, C.A.S. Almeida, Phys. Rev. D 88 (2013) 025005.
- [58] Z. Li, A. Övgün, Phys. Rev. D 101 (2020) 024040.
- [59] R. Bluhm, N.L. Gagne, R. Potting, A. Vrublevskis, Phys. Rev. D 77 (2008) 125007.
- [60] C. A. Escobar, A. Martín-Ruiz, Phys. Rev. D 95 (2017) 095006.
- [61] R.V. Maluf, J.E.G. Silva, C.A.S. Almeida, Phys. Lett. B 749 (2015) 304.
- [62] C. Hernaski, Phys. Rev. D 90 (2014) 124036.
- [63] S.M. Carroll, T.R. Dulaney, M.I. Gresham, H. Tam, Phys.Rev.D 79 (2009) 065011.
- [64] R. Casana, A. Cavalcante, F.P. Poulis, E.B. Santos, Phys. Rev. D 97 (2018) 104001.
- [65] A. Övgün, K. Jusufi, I. Sakalli, Phys. Rev. D 99 (2019) 024042.
- [66] C. Ding, C. Liu, R. Casana, A. Cavalcante, Eur. Phys. J. C 80 (2020) 178.
- [67] A.F. Santos, A.Y. Petrov, W.D.R. Jesus, J. R. Nascimento, Mod. Phys. Lett. A 30 (2015) 1550011.
- [68] S.K. Jha, A. Rahaman, Eur. Phys. J. C 81 (2021) 345.
- [69] A.A.A. Filho, J.R. Nascimento, A.Y. Petrov, P.J. Porfírio, Phys. Rev. D 108 (2023) 085010.
- [70] R. Xu, D. Liang, L. Shao, Phys. Rev. D 107 (2023) 024011.
- [71] C. Ding, Y. Shi, J. Chen, Y. Zhou, C. Liu, Y. Xiao, Eur. Phys. J. C 83 (2023) 573.
- [72] Y.S. Priyobarta, T.S. Ibungochouba, Eur. Phys. J. C 84 (2024) 1245.
- [73] A. Uniyal, S. Kanzi, I. Sakalli, Eur. Phys. J. C. 83 (2023)668.
- [74] C. Chen, Q. Pan, J. Jing, Phys. Lett. B 846 (2023) 138186.
- [75] R. H. Lin, R. Jiang, X.H. Zhai, Eur. Phys. J. C. 83 (2023)720.
- [76] H. Wang, S. Wei, Eur. Phys. J. Plus 137 (2022) 571.
- [77] R. Jiang, R. Lin, X. Zhai, Phys. Rev. D 104 (2021) 124004.
- [78] C. Liu, C. Ding, J. Jing, arXiv :1910.13259 [gr -qc].
- [79] S.E. Motta, T.M. Belloni, L. Stella, et al., Mon. Not. R. Astron. Soc. 437 (2014) 2554.
- [80] J.A. Orosz, J.F. Steiner, J.E. McClintock, et al., Astrophys. J. 730 (2011) 75.
- [81] M.J. Reid, J.E. McClintock, J.F. Steiner, et al., Astrophys. J. 796 (2014) 2.
- [82] T.W.B. Kibble, J. Phys. A 9 (1976) 1387.
- [83] Q. Pan, J. Jing, Class. Quantum Gravity 25 (2008) 038002.
- [84] S. Chen, J. Jing, Mod. Phys. Lett. A 23 (2008) 359.
- [85] I. Güllü, A. Övgün, Annals Phys. 436 (2022) 168721.
- [86] J.L. Synge, Mon. Not. R. Astron. Soc. 131 (1966) 463.
- [87] J.P. Luminet, Astron. Astrophys. 75 (1979) 228.
- [88] J.M. Bardeen, in Proceedings, Ecole d'Été de Physique Théorique: Les Astres Occlus : Les Houches, France, August, 1972 (1973) 215–240.
- [89] K. Akiyama et al. [Event Horizon Telescope], Astrophys. J. Lett. 930 (2) (2022) L12.
- [90] V.I. Dokuchaev, N.O. Nazarova, Universe 6 (2020) 154.
- [91] A. Higuchi, Class. Quantum Gravity 18 (2001) L139.
- [92] P. Kanti, J. March-Russell, Phys. Rev. D 66 (2002) 024023.
- [93] E. Jung, D.K. Park, Class. Quantum Gravity 21 (2004) 3717.
- [94] J. Grain, A. Barrau, P. Kanti, Phys. Rev. D 72 (2005) 104016.
- [95] L.C.B. Crispino, E.S. Oliveira, A. Higuchi, G.E.A. Matsas, Phys. Rev. D 75 (2007) 104012.
- [96] L.C.B. Crispino, S.R. Dolan, E.S. Oliveira, Phys. Rev. D 79 (2009) 064022.
- [97] C.F.B. Macedo, L.C.B. Crispino, Phys. Rev. D 90 (2014) 064001.
- [98] H. Huang, M. Jiang, J. Chen, Y. Wang, Gen. Relativ. Gravit. 47 (2015) 8.
- [99] L.C.S. Leite, S. Dolan, L. Crispino, C.B., Phys. Rev. D 98 (2018) 024046.
- [100] H. Huang, J. Chen, Y. Wang, T. Lu, Gen. Relativ. Gravit. 51 (2019) 22.
- [101] M.A. Anacleto, F.A. Brito, J.A.V. Campos, E. Passos, Phys. Lett. B 803 (2020) 135334.
- [102] R.B. Magalhães, L.C.S. Leite, L.C.B. Crispino, Eur. Phys. J. C 80 (2020) 386.
- [103] H.C.D. Lima, C.L. Benone, L.C.B. Crispino, Phys. Lett. B 811 (2020) 135921.
- [104] C.L. Benone, L.C.S. Leite, L.C.B. Crispino, S.R. Dolan, Int. J. Mod. Phys. D 27 (2018) 1843012.
- [105] Q. Li, C. Ma, Y. Zhang, Z.W. Lin, P.F. Duan, Chin. J. Phys. 77 (2022) 1269.
- [106] T.S. Ibungochouba, I.M. Ablu, K.S. Yugindro, Int. J. Mod. Phys. D 25 (2016) 1650061.
- [107] S. Devi, R. Roy, S. Chakrabarti, Eur. Phys. J. C. 80 (2020) 760.
- [108] D. J. Gogoi, A. Övgün, D. Demir, Phys. Dark Universe. 42 (2023) 101314.
- [109] D. J. Gogoi, U. D. Goswami, J. Cosmol. Astropart. Phys. 06 (2022) 029.
- [110] T.S. Ibungochouba, Chin. Phys. B 24 (2015) 070401.
- [111] X. Zhang, M. Wang, J. Jing, Sci. China-Phys. Mech. Astron. 64 (2021) 250411.
- [112] J.A. Wheeler, Academic Press, New York, NY, USA, (1973)
- [113] A.R. Ruffini, Gordon and Breach Science Publishers, New York, NY, USA, (1973)
- [114] S. Chandrasekhar, The Mathematical Theory of Black Holes, Clarendon Press, Oxford (1983).

- [115] E. Newman, R. Penrose, J. Math. Phys. 7 (1966) 863.
- [116] J.N. Goldberg, A.J. Macfarlane, E. Newman, F. Rohrlich, E.C.G. Sudarshan, J. Math. Phys. 8 (1967) 2155.
- [117] B.F. Schutz, C.M. Will, Astrophys. J. Lett. 291 (1985) L33.
- [118] R.A. Konoplya, Phys. Rev. D 68, (2003) 024018.
- [119] J. Matyjasek, M. Opala, Phys. Rev. D 96 (2017) 024011.
- [120] J. Matyjasek, M. Telecka, Phys. Rev. D 100 (2019) 124006.
- [121] R.A. Konoplya, Phys. Lett. B 804 (2020) 135363.
- [122] N. G. Sanchez, Phys. Rev. D 18 (1978) 1030.
- [123] S. R. Das, G. W. Gibbons, S. D. Mathur, Phys. Rev. Lett. 78 (1997) 417.
- [124] Y. Decanini, G. Esposito-Farese, A. Folacci, Phys. Rev. D 83 (2011) 044032.
- [125] Y. Décanini, A. Folacci, B. Raffaelli, Phys. Rev. D 81 (2010) 104039.